UNIVERSITY OF CAGLIARI

PHD COURSE IN ELECTRONIC AND COMPUTER ENGINEERING

CLASS XXX (ING-IND/32)

DESIGN & CONTROL OF HIGH-SPEED PMSM

AUTHOR: GIUSEPPE FOIS

PHD COURSE COORDINATOR: PROF. FABIO ROLI

ADVISOR: PROF. ALFONSO DAMIANO

CO-ADVISOR: DR. ALESSANDRO SERPI

ACADEMIC YEAR 2016-2017

FEBRUARY-MARCH 2018 SESSION

ABSTRACT

In this PhD dissertation the design of a novel High-Speed Ferrite-based Permanent Magnet Synchronous Machine suitable for automotive application is presented. In particular, a sleeved surface-mounted HS-PMSM configuration has been chosen, since it enables higher peripheral speeds compared to the other configurations. Therefore, mechanical and electromagnetic modelling has been considered at first, based on which the design of the HS-PMSM has been carried out. This is done through a novel multi-parameter analytical design procedure, which has been developed with the aim of achieving a preliminary machine design that takes into account both design targets and constraints; the former have been set in accordance with electric vehicle application requirements, whereas operating constraints are related mainly to high-speed operation and PM demagnetization issues. The proposed design approach has been validated through extensive simulation studies, which have been performed by means of Finite Element Analyses (FEAs) that regard both mechanical and electromagnetic aspects. In addition, a Permanent Magnet Brushless DC Machine (PMBDCM) configuration has been chosen with the aim of achieving higher torque density and/or lower Joule losses compared to Permanent Magnet Brushless AC Machines (PMBACMs). In this regard, the second part of this PhD dissertation focuses on an improved three-phase-on (3PO) control approach, which benefits from appropriate zero-sequence currents in order to further increase PMBDCM exploitation. In particular, the injection of a suitable zero-sequence current allows a further reduction of Joule losses compared to those achievable by means of the original 3PO. Furthermore, a suitable Space Vector Control (SVC) has been developed based on a novel synchronous reference frame, which has been defined in accordance with the 3PO control approach previously mentioned. The effectiveness of the proposed SVC in driving the designed HS-PMSM has been verified through numerical simulations, which have been carried out in the Matlab Simulink environment. These regard also the implementation of a conventional Current Commutation Control for comparison purposes.

GIUSEPPE FOIS gratefully acknowledges Sardinia Regional Government for the financial support of his PhD scholarship (P.O.R. Sardegna F.S.E. Operational Programme of the Autonomous Region of Sardinia, European Social Fund 2007-2013 - Axis IV Human Resources, Objective l.3, Line of Activity l.3.1.)

REGIONE AUTÒNOMA DE SARDIGNA
REGIONE AUTONOMA DELLA SARDEGNA

OUTLINE

I. INTRODUCTION

Permanent Magnet Synchronous Machines (PMSMs) are nowadays widely employed as either motors or generators in a large variety of applications, ranging from distributed power generation, such as wind and hydro turbines, to electric propulsion systems for electric and hybrid electric vehicles [1]–[4]. Such a wide employment is mainly due to Permanent Magnet (PM) excitation, which enables high torque and power density, low maintenance, high efficiency and reliability. These advantages are achieved resorting to appropriate PM materials and machine topologies [5]–[7]. In this context, rare-earth PMs are typically used due to their high-energy density, which leads to high airgap magnetic flux density with small amount of PMs. Consequently, the employment of rare-earth PMs limits machine rotor size and weights and, thus, peripheral speed. However, there is a great concern about using rare-earth PMs due to availability and price fluctuation issues. In addition, this kind of PMs suffers from relatively low maximum operating temperature. Consequently, the use of less rare-earth or no rare-earth PMs, such as ferrite PMs, have been proposed recently as a viable and alternative solution [8], [9], especially in growing sectors as automotive [10]. However, ferrite-based PMSMs still suffer from relatively low torque and power density, as well as from some critical issues related to weak residual magnetism and low coercive force.

The employment of ferrite PMs seems particularly suitable for High-Speed Permanent Magnet Synchronous Machines (HS-PMSMs), which are characterized by rated speed

from 10 krpm to over 200 krpm and rated power from few watts to hundreds of kilowatts. Therefore, since HS-PMSM does not need high airgap flux density due to the very high rotational speed, using ferrite PMs may enable significant cost saving compared to other solutions [8], [11]. The HS-PMSM has been widely employed for a long time due to its numerous advantages, among which high power density and efficiency, reduced size, weights and overall costs. At the present time, HS-PMSMs are employed in a wide range of applications, such as dental drills and medical surgery tools, flywheel energy storage systems, gas and oil compressors, spindles and for power generation [12]–[14]. In these applications, the employment of a high-speed electrical machine allows the elimination of gear boxes for increasing the motor speed to the that required by the load, leading to reduced weight and size, lower noise, higher efficiency and less maintenance needs [12]. Furthermore, HS-PMSMs are becoming recently a promising solution also in those fields in which low sizes and weights, together with high efficiencies, are of significant importance. This is because novel materials and recent improvements in power electronics and control systems are enabling a further increase of HS-PMSM performances and speed operating range [15], making them suitable also for electric propulsion systems.

One of the main challenges in designing an HS-PMSM is surely the high mechanical forces acting on the rotor due to the high rotational speed, which must be taken into account properly. In this regard, it is worth noting that the surface-mounted permanent magnet synchronous machine is the best configuration in terms of maximum peripheral speed as far as an appropriate sleeve is concerned [16]. In particular, the PMs are usually glued to the rotor shaft and contained by mechanical sleeves made up of high-strength materials, such as metallic alloys or carbon fibers [17]. Consequently, rotor design should be accomplished by guaranteeing PM integrity and containment at any operating condition. In addition, PM demagnetization has to be avoided properly, especially when low energy density PMs are employed. Another main challenge in designing HS-PMSM for electric propulsion systems is the need for high gear ratios in order to guarantee an appropriate coupling between HS-PMSM rotor and vehicle wheels. The use of a single mechanical gear characterized by a high gear ratio does not seem a suitable solution because it increases volume and weight of the propulsion system significantly, reducing its overall efficiency as well. Alternatively, multiple mechanical gears with relatively low gear ratios may be employed, which are series-connected in order to enable a sequential reduction of HS-PMSM speed. This configuration limits volume and weight increase compared to the previous solution, as pointed out in [18], but still suffers from efficiency issues due to high mechanical losses. A very promising solution consists of magnetic gears, which are characterized by high gear ratios, reduced volume and weight, as well as

by high efficiency. As a result, the use of HS-PMSM combined with a suitable transmission system (series-connected and/or magnetic) allows a 20% reduction of volume and weight of electric propulsion system for electric vehicle compared to those actually available on the market [18].

Regarding HS-PMSM control system, two main current control approaches have been proposed in the literature [19]–[21], namely Brushless AC (BLAC) or Brushless DC (BLDC). BLAC consists of modulating phase currents appropriately and, thus, it is generally employed for PMSM characterized by sinusoidal-shaped back-emfs (Permanent Magnet Brushless AC Machines, PMBACMs). As a result, PMBACMs are generally driven by Space Vector Control (SVC), which relies on high-resolution position sensors in order to assure high performances and low torque ripple. Whereas BLDC is generally employed for PMSM characterized by trapezoidal-shaped back-emfs (Permanent Magnet Brushless DC Machines, PMBDCMs); this control approach consists of injecting suitable constant currents in accordance with the trapezoidal shapes of the PMBDCM back-emfs (Current Commutation Control, CCC). Therefore, CCC is quite simple, effective and easy to be implemented, requiring low-resolution position sensors only. However, unsuitable torque ripple occurs over the periodical current commutations, which has to be minimized in order to assure adequate PMBDCM performances [22]–[25]. However, since PMBDCMs are characterized by higher potential performances compared to PMBACMs, especially in terms of torque density, some alternative PMBDCM control approaches have been proposed in the literature [26]–[28], which aim to increase PMBDCM performances and exploitation by means of suitable reference phase currents. Among these, the three-phase-on control approach (3PO) proposed in [27] seems to be quite promising; this resorts to three-phase current supply in order to increase PMBDCM performances and exploitation compared to CCC, especially in terms of torque ripple, average torque and Joule losses [28]. Although such a high-performance control approach may require the employment of high-resolution position sensors, this can be avoided resorting to appropriate sensorless algorithms, whose effectiveness can be achieved also in the case of un-ideal trapezoidal-shaped back-emfs [29], [30].

In this scenario, this PhD dissertation presents the design of a novel High-Speed Ferrite-based Permanent Magnet Synchronous Machine suitable for automotive application. In particular, a sleeved surface-mounted HS-PMSM configuration has been chosen, since it enables higher peripheral speeds compared to the other configurations [16]. Therefore, mechanical and electromagnetic modelling has been considered at first, based on which the design of the HS-PMSM has been carried out. This is done through a novel multi-parameter analytical design procedure, which has been developed with the aim of achieving a preliminary machine design that takes into account both design targets

and constraints; the former have been set in accordance with electric vehicle application requirements, whereas operating constraints are related mainly to high-speed operation and PM demagnetization issues. The proposed design approach has been validated through extensive simulation studies, which have been performed by means of Finite Element Analyses (FEAs) that regard both mechanical and electromagnetic aspects. In addition, a PMBDCM configuration has been chosen with the aim of achieving higher torque density and/or lower Joule losses compared to PMBACMs. In this regard, the second part of this PhD dissertation focuses on an improved 3PO control approach, which benefits from appropriate zero-sequence currents in order to further increase PMBDCM exploitation. In particular, the injection of a suitable zero-sequence current allows a further reduction of Joule losses compared to those achievable by means of the original 3PO. Furthermore, a suitable SVC has been developed based on a novel synchronous reference frame, which has been defined in accordance with the 3PO control approach previously mentioned. The effectiveness of the proposed SVC in driving the designed HS-PMSM has been verified through numerical simulations, which have been carried out in the Matlab Simulink environment. These regard also the implementation of a conventional CCC for comparison purposes.

II. HIGH-SPEED PMSM – DESIGN

The design of High-Speed Permanent Magnet Synchronous Machine (HS-PMSM) has to address some critical aspects; these are due mainly to the very high rotational speed, which causes high mechanical stress at high frequency. Therefore, differently from low-speed PMSM, the mechanical modelling plays a crucial role in HS-PMSM, it being even more important than the electromagnetic one. In this regard, once the HS-PMSM topology is chosen, the mechanical modelling of the rotor is fundamental in order to define appropriate mechanical constraints; these affect the HS-PMSM rotor geometry, especially the choice of PM materials and their displacement. In fact, PM materials generally present better mechanical properties to compression stress rather than to tensile stress. Therefore, for an inner rotor HS-PMSM configuration, the PMs should be contained by a mechanical sleeve in order to limit tensile stress and guarantee their retention, especially at high-speed operation [31]–[33].

Apart from mechanical aspects, electromagnetic modeling is also very important for HS-PMSMs, especially when ferrite PMs are employed. In particular, due to low residual magnetic flux density and coercive force, PM demagnetization has to be avoided at any operating conditions. For this purpose, the magnetic flux path has to be considered carefully, as well as the effects of stator winding supply. In addition, as far as a mechanical sleeve is concerned, it acts as an additional airgap from a magnetic point of view. Consequently, sleeve thickness has to be chosen not only based on mechanical

needs, but also in order to prevent an excessive airgap length, which would cause weak magnetic flux density. In this regard, it is worth noting that magnetic flux density could be increased by increasing PM volume; however, this would lead to increased sleeve thickness. Consequently, an integrated mechanical-electromagnetic design procedure should be adopted.

Based on the previous considerations, both mechanical and electromagnetic models have been considered at first, which are presented in the following sections.

II.1. Mechanical Modeling

The mechanical modeling has been developed referring to the HS-PMSM structure shown in Fig. 1, all the symbols of which are defined in TABLE I. The rotor is made up of an inner shaft, a middle layer of electrical steel, a ferrite PM ring and an outer sleeve. In addition, in order to increase mechanical retention, the sleeve is prestressed and mounted forcibly, making a mechanical pretension acting on the PMs.

In order to investigate mechanical stresses acting on HS-PMSM rotor, reference has to be made to all its layers, which are made up of different materials and characterized by different thicknesses. In particular, each rotor layer can be considered as a rotating cylinder. Consequently, mechanical modelling of this specific geometric structure is introduced at first in order to determine radial and tangential stresses on both inner and outer surfaces. This formulation can be then applied to the HS-PMSM rotor in order to assess PM retention at any speed and temperature within the given operating ranges.

II.1.1. Rotating cylinder

Referring to the schematic representation of a generic rotating cylinder shown in Fig. 2, it is assumed that the shear stresses can be neglected and that the internal stress is due to radial and tangential strains only. Considering the cylinder material homogeneous and isotropic, the Hooke's Law can be applied to its generic infinitesimal portion depicted in Fig. 2, leading to

$$\varepsilon_r = \frac{du_r}{dr} = \frac{1}{E_Y}\sigma_r - \frac{\upsilon}{E_Y}\sigma_\theta + \alpha_T \Delta T \tag{II.1.1}$$

$$\varepsilon_\theta = \frac{u_r}{r} = -\frac{\upsilon}{E_Y}\sigma_r + \frac{1}{E_Y}\sigma_\theta + \alpha_T \Delta T \tag{II.1.2}$$

where ε_r and ε_θ are the tangential and radial strains due to the radial displacement u_r.

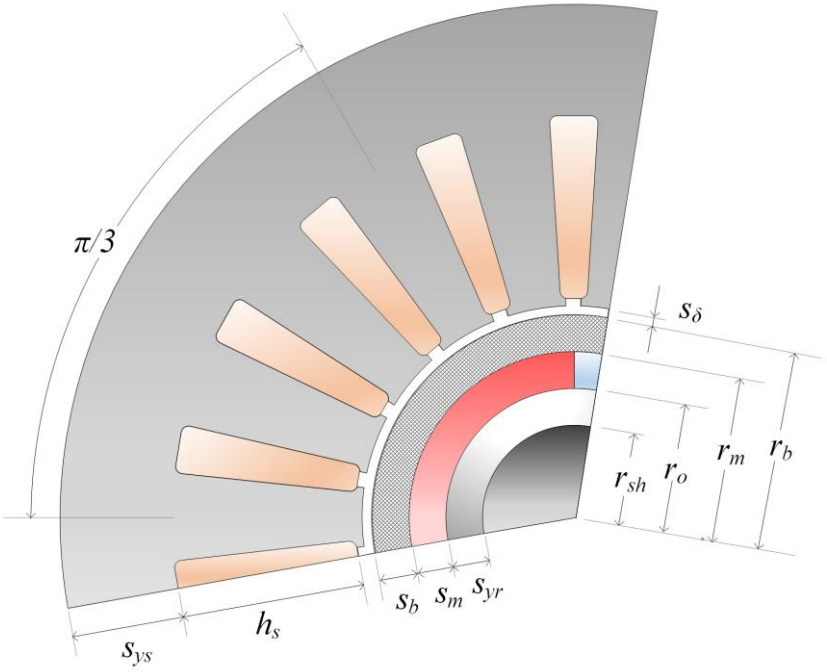

Fig. 1 Structure of the HS-PMSM.

TABLE I HS-PMSM NOMENCLATURE

Variable	**Symbol**
Shaft radius	r_{sh}
Outer rotor iron radius	r_o
Outer magnet radius	r_m
Outer sleeve radius	r_s
Rotor yoke thickness	s_{yr}
PM thickness	s_m
Sleeve thickness	s_b
Air-gap	s_δ
Stator outer radius	r_s
Stator yoke	s_{ys}
Slot height	h_s
Active length	l_i

Furthermore, σ_r and σ_θ denote the radial and tangential stresses, while E_Y and υ are Young's modulus and Poisson's ratio respectively. Still referring to (II.1.1) and (II.1.2), α_T is the thermal expansion coefficient, which may determine additional strains depending on the difference between actual and reference temperatures (ΔT).

Referring to σ_r and σ_θ, they depend on each other through the equilibrium equation of

the Theory of Elastic Mechanics as

$$\sigma_r + r\frac{d\sigma_r}{dr} - \sigma_\theta + \rho\omega_m^2 r^2 = 0 \qquad \text{(II.1.3)}$$

where r is the radius of the infinitesimal portion of the cylinder, ρ is its density and ω_m is the rotational speed. By properly combining (II.1.1) and (II.1.2) with (II.1.3), the radial stress equation is achieved as

$$\frac{d^2\sigma_r}{dr^2} + \frac{3}{r}\frac{d\sigma_r}{dr} + (3+\upsilon)\rho\omega_m^2 + \frac{E_Y\alpha_T}{r}\frac{d\Delta T}{dr} = 0\,. \qquad \text{(II.1.4)}$$

In addition, using the superimposition principle, σ_r can be split into three components, which depend only on rotational speed ($\sigma_{r,\omega}$), temperature variation ($\sigma_{r,T}$) and contact pressures ($\sigma_{r,p}$) respectively:

$$\sigma_r = \sigma_{r,p} + \sigma_{r,\omega} + \sigma_{r,T}\ . \qquad \text{(II.1.5)}$$

Pressure component ($\sigma_{r,p}$) can be obtained from (II.1.4) by imposing ω_m equal to zero and no temperature variation with r, leading to

$$\frac{d^2\sigma_{r,p}}{dr^2} + \frac{3}{r}\frac{d\sigma_{r,p}}{dr} = 0\,. \qquad \text{(II.1.6)}$$

Therefore, (II.1.6) can be integrated twice within $[r_i,r_o]$, where r_i and r_o are the inner and outer radii of the cylinder, by considering the following boundary conditions:

$$\sigma_{r,p}(r_i) = -p_i\,, \quad \sigma_{r,p}(r_o) = p_o \qquad \text{(II.1.7)}$$

where p_i and p_o are the pressure acting on inner and outer cylinder surfaces respectively, as highlighted in Fig. 2. As a result, the following expression is achieved:

$$\sigma_{r,p} = \frac{p_i r_i^2 - p_o r_o^2 + (p_o - p_i)\left(\frac{r_i r_o}{r}\right)^2}{r_o^2 - r_i^2}\,. \qquad \text{(II.1.8)}$$

Similarly to $\sigma_{r,p}$, $\sigma_{r,\omega}$ is determined by imposing no temperature variation in (II.1.4) and assuming no external pressure acting on cylinder surfaces as boundary conditions:

$$\frac{d^2\sigma_{r,\omega}}{dr^2} + \frac{3}{r}\frac{d\sigma_{r,\omega}}{dr} + (3+\upsilon)\rho\omega_m^2 = 0\,, \quad \sigma_{r,\omega}(r_i) = \sigma_{r,\omega}(r_o) = 0\,. \qquad \text{(II.1.9)}$$

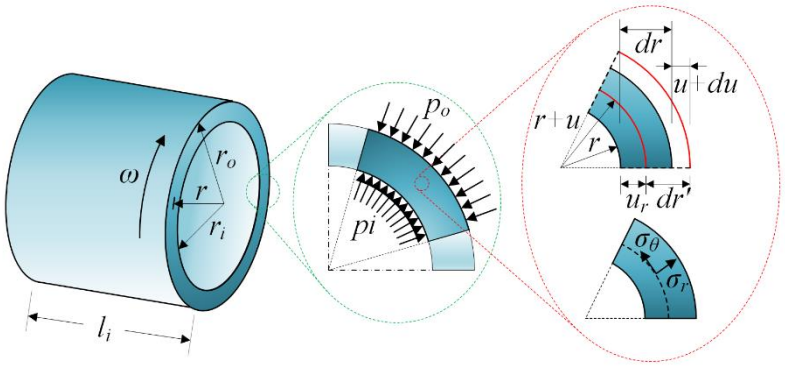

Fig. 2 Representation of the rotating cylinder and of its infinitesimal portion, where p_i and p_o denote internal and external pressures respectively.

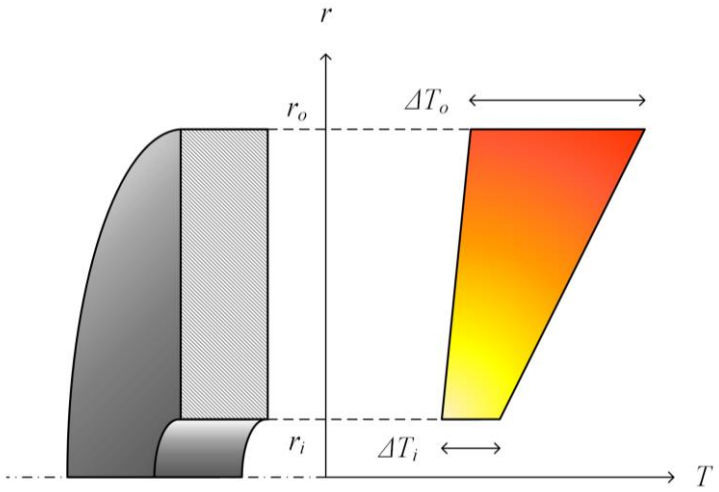

Fig. 3 The temperature distribution within the rotating cylinder.

Consequently, by integrating (II.1.9) within $[r_i,r_o]$, the following result is achieved:

$$\sigma_{r,\omega} = \left(\frac{3+\upsilon}{8}\right)\left(\left(r_o{}^2 + r_i^2\right) - \left(\frac{r_i r_o}{r}\right)^2 - r^2\right)\rho\omega_m^2 . \qquad \text{(II.1.10)}$$

In order to determine $\sigma_{r,T}$, a linear temperature distribution within the cylinder is assumed, as depicted in Fig. 3 and stated by the following equation:

$$\Delta T = k_0 + k_1 r \qquad \text{(II.1.11)}$$

where ΔT is the difference between the temperature before and after the deformation. While k_0 and k_1 are defined as

$$k_0 = \Delta T_o - \frac{\Delta T_o - \Delta T_i}{r_o - r_i} r_o , \quad k_1 = \frac{\Delta T_o - \Delta T_i}{r_o - r_i} \qquad \text{(II.1.12)}$$

where ΔT_i and ΔT_o are the temperature of the inner and outer surface of the considered cylinder with respect to a common reference temperature. Hence, considering no pressure and speed, (II.1.4) becomes

$$\frac{d^2\sigma_{r,T}}{dr^2}+\frac{3}{r}\frac{d\sigma_{r,T}}{dr}+\frac{E_Y\alpha_T}{r}\frac{d\Delta T}{dr}=0\,,\quad \sigma_{r,T}\left(r_i\right)=\sigma_{r,T}\left(r_o\right)=0\,. \tag{II.1.13}$$

Therefore, by substituting (II.1.11) in (II.1.13) and integrating the latter within $[r_i,r_o]$, the following result is achieved

$$\sigma_{r,T}=\frac{E_Y\alpha_T}{3}\frac{k_1}{r_o+r_i}\left(r_o^{\,2}+r_i^{\,2}+r_or_i-\frac{r_o^{\,2}r_i^{\,2}}{r^2}-r\left(r_o+r_i\right)\right). \tag{II.1.14}$$

Based on (II.1.8), (II.1.10) and (II.1.14), it is possible to compute the corresponding tangential stress components by means of (II.1.3), leading to

$$\sigma_\theta=\sigma_{\theta,p}+\sigma_{\theta,\omega}+\sigma_{\theta,T} \tag{II.1.15}$$

in which

$$\sigma_{\theta,p}=\frac{p_ir_i^{\,2}-p_or_o^{\,2}-\left(p_o-p_i\right)\left(\frac{r_ir_o}{r}\right)^2}{r_o^{\,2}-r_i^{\,2}} \tag{II.1.16}$$

$$\sigma_{\theta,\omega}=\left(\frac{3+\upsilon}{8}\right)\left(\left(r_o^{\,2}+r_i^{\,2}\right)+\left(\frac{r_ir_o}{r}\right)^2-\frac{1+3\upsilon}{3+\upsilon}r^2\right)\rho\omega_m^2 \tag{II.1.17}$$

$$\sigma_{\theta,T}=\frac{E_Y\alpha_T}{3}\frac{k_1}{r_o+r_i}\left(r_o^{\,2}+r_i^{\,2}+r_or_i+\frac{r_o^{\,2}r_i^{\,2}}{r^2}-2r\left(r_o+r_i\right)\right). \tag{II.1.18}$$

In conclusion, it is worth noting that both σ_r and σ_θ contribute to determine the Von Mises equivalent stress, which can be computed as

$$\sigma_{eq}=\sqrt{\sigma_r^{\,2}+\sigma_\theta^{\,2}-\sigma_r\sigma_\theta}\,. \tag{II.1.19}$$

II.1.2. High-Speed PMSM rotor

Once the mechanical modeling of a generic rotating cylinder has been defined, it is possible to carry out a mechanical stress analysis on the HS-PMSM rotor. For this purpose, reference is made to Fig. 4, which highlights the main dimensions of the three

rotor layers. In particular, rotor shaft and back-iron have been considered as a single layer (L1) because their materials are very similar to each other from a mechanical point of view.

In addition, the sleeve (L3) is prestressed in order to assure PM retention at any speed, especially at high-speed operation; this means that the inner radius of the sleeve surrounding the PMs (r_m) is greater than its free inner radius (r_{bi}), as highlighted in Fig. 4. This shows the interference fit (δ), which is the difference between the outer radius of the PM ring (L2) and the free inner radius of the sleeve.

Hence, in order to apply (II.1.19), radial and tangential stresses on each layer have to be determined by means of (II.1.5) and (II.1.15). This requires the knowledge of all σ_r and σ_θ components, which can be computed in accordance with (II.1.8), (II.1.10), (II.1.14) and (II.1.16)-(II.1.18), all these equations being summed up in TABLE II. In this regard, appropriate constraints have to be imposed in terms of pressure and interference on the contact surfaces of each rotor layer. Therefore, referring to contact pressures at first, the following relationships can be imposed:

$$\begin{aligned} &p_i^{(L1)} = 0\,, \quad p_o^{(L3)} = 0 \\ &p_o^{(L1)} = -p_i^{(L2)}\,, \quad p_o^{(L2)} = -p_i^{(L3)}\,. \end{aligned} \tag{II.1.20}$$

Therefore, based on (II.1.20), only internal and external pressures acting on the PM ring (L2) have to be determined, the other ones resulting from boundary and continuity constraints imposed by (II.1.20). These pressures can be computed by considering the continuity constraints on the radial displacements between each pair of adjacent layers:

$$u_r^{(L3)} - u_r^{(L2)}\Big|_{r=r_m} = \delta\,, \quad u_r^{(L2)} - u_r^{(L1)}\Big|_{r=r_o} = 0\,. \tag{II.1.21}$$

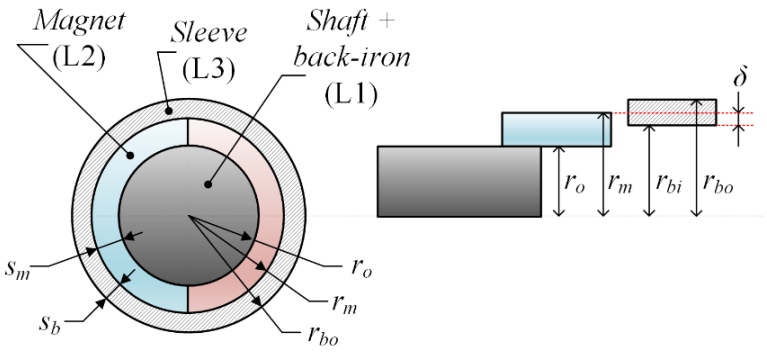

Fig. 4 Cross section of the rotor: shaft and rotor back-iron, PMs and sleeve.

Hence, by substituting (II.1.2) in (II.1.21) and by taking into account (II.1.20) and all the expressions reported in TABLE II, the following equations are achieved:

$$\begin{aligned} K_1 p_o^{(L2)} + K_2 p_i^{(L2)} + C_{\omega 1} + C_{T1} &= \delta \\ K_3 p_o^{(L2)} + K_4 p_i^{(L2)} + C_{\omega 2} + C_{T2} &= 0 \end{aligned} \tag{II.1.22}$$

where the *K* and *C* coefficients depend on rotor parameters, material properties, rotational speed and operating temperature, as reported below:

TABLE II RADIAL AND TANGENTIAL STRESS EQUATIONS

Reference	Symbol	Equation
(II.1.5)	σ_r	$\sigma_r = \sigma_{r,p} + \sigma_{r,\omega} + \sigma_{r,T}$
(II.1.8)	$\sigma_{r,p}$	$\sigma_{r,p} = \dfrac{p_i r_i^2 - p_o r_o^2 + (p_o - p_i)\left(\dfrac{r_i r_o}{r}\right)^2}{r_o^2 - r_i^2}$
(II.1.10)	$\sigma_{r,\omega}$	$\sigma_{r,\omega} = \left(\dfrac{3+\upsilon}{8}\right)\left((r_o^2 + r_i^2) - \left(\dfrac{r_i r_o}{r}\right)^2 - r^2\right)\rho\omega_m^2$
(II.1.14)	$\sigma_{r,T}$	$\sigma_{r,T} = \dfrac{E_Y \alpha_T}{3}\dfrac{k_1}{r_o + r_i}\left(r_o^2 + r_i^2 + r_o r_i - \dfrac{r_o^2 r_i^2}{r^2} - r(r_o + r_i)\right)$
(II.1.15)	σ_θ	$\sigma_\theta = \sigma_{\theta,p} + \sigma_{\theta,\omega} + \sigma_{\theta,T}$
(II.1.16)	$\sigma_{\theta,p}$	$\sigma_{\theta,p} = \dfrac{p_i r_i^2 - p_o r_o^2 - (p_o - p_i)\left(\dfrac{r_i r_o}{r}\right)^2}{r_o^2 - r_i^2}$
(II.1.17)	$\sigma_{\theta,\omega}$	$\sigma_{\theta,\omega} = \left(\dfrac{3+\upsilon}{8}\right)\left((r_o^2 + r_i^2) + \left(\dfrac{r_i r_o}{r}\right)^2 - \dfrac{1+3\upsilon}{3+\upsilon} r^2\right)\rho\omega_m^2$
(II.1.18)	$\sigma_{\theta,T}$	$\sigma_{\theta,T} = \dfrac{E_Y \alpha_T}{3}\dfrac{k_1}{r_o + r_i}\left(r_o^2 + r_i^2 + r_o r_i + \dfrac{r_o^2 r_i^2}{r^2} - 2r(r_o + r_i)\right)$

$$K_1 = \frac{r_m}{E_Y^{(L3)}}\left(\frac{r_s^{\,2} + r_m^{\,2}}{r_s^{\,2} - r_m^{\,2}} + \upsilon^{(L3)}\right) + \frac{r_m}{E_Y^{(L2)}}\left(\frac{r_m^{\,2} + r_o^{\,2}}{r_m^{\,2} - r_o^{\,2}} - \upsilon^{(L2)}\right) \tag{II.1.23}$$

$$K_2 = -\frac{r_m}{E_Y^{(L2)}}\left(\frac{2r_o^{\,2}}{r_m^{\,2} - r_o^{\,2}}\right) \tag{II.1.24}$$

$$K_3 = -\frac{r_o}{E_Y^{(L2)}}\left(\frac{2r_m^{\,2}}{r_m^{\,2} - r_o^{\,2}}\right) \tag{II.1.25}$$

$$K_4 = \frac{r_o}{E_Y^{(L2)}}\left(\frac{r_m^{\,2} + r_o^{\,2}}{r_m^{\,2} - r_o^{\,2}} + \upsilon^{(L2)}\right) + \frac{r_o}{E_Y^{(L1)}}\left(1 - \upsilon^{(L1)}\right) \tag{II.1.26}$$

$$C_{\omega 1} = \frac{\omega_m^{\,2}}{4}\left(\begin{array}{l} \frac{r_m}{E_s}\left(\left(3+\upsilon^{(L3)}\right)r_s^{\,2} + \left(1-\upsilon^{(L3)}\right)r_m^{\,2}\right)\rho^{(L3)} + \\ -\frac{r_m}{E_Y^{(L2)}}\left(\left(3+\upsilon_m\right)r_o^{\,2} + \left(1-\upsilon^{(L2)}\right)r_m^{\,2}\right)\rho^{(L2)} \end{array}\right) \tag{II.1.27}$$

$$C_{\omega 2} = \frac{\omega_m^{\,2}}{4}\left(\begin{array}{l} \frac{r_o}{E_Y^{(L2)}}\left(\left(3+\upsilon^{(L2)}\right)r_o^{\,2} + \left(1-\upsilon^{(L2)}\right)r_m^{\,2}\right)\rho^{(L2)} + \\ -\frac{r_o}{E_Y^{(L1)}}\left(\left(1-\upsilon^{(L1)}\right)r_o^{\,2}\right)\rho^{(L1)} \end{array}\right) \tag{II.1.28}$$

$$C_{T1} = r_m\left(\begin{array}{l} \frac{\left(\Delta T_o^{(L3)} - \Delta T_i^{(L3)}\right)\alpha_T^{(L3)}}{3}\left(1 + \frac{r_b}{r_b + r_m}\right) + \alpha_T^{(L3)}\Delta T + \\ + \frac{\left(\Delta T_o^{(L2)} - \Delta T_i^{(L2)}\right)\alpha_T^{(L2)}}{3}\left(1 + \frac{r_o}{r_m + r_o}\right) - \alpha_T^{(L2)}\Delta T \end{array}\right) \tag{II.1.29}$$

$$C_{T2} = r_{yr}\left(\begin{array}{l} \frac{\left(\Delta T_o^{(L2)} - \Delta T_i^{(L2)}\right)\alpha_T^{(L2)}}{3}\left(1 + \frac{r_m}{r_m + r_o}\right) + \alpha_T^{(L2)}\Delta T + \\ + \frac{\left(\Delta T_o^{(L1)} - \Delta T_i^{(L1)}\right)\alpha_T^{(L1)}}{3} - \alpha_T^{(L1)}\Delta T \end{array}\right). \tag{II.1.30}$$

As a result, the contact pressures on the PM ring can be computed by solving (II.1.22) as

$$\begin{aligned} p_i^{(L2)} &= \frac{-C_{\omega 2}K_1 + C_{\omega 1}K_3 - \delta K_3 + C_{T1}K_3 - C_{T2}K_1}{K_1K_4 - K_3K_2} \\ p_o^{(L2)} &= \frac{C_{\omega 2}K_2 - C_{\omega 1}K_4 + \delta K_4 - C_{T1}K_4 + C_{T2}K_2}{K_1K_4 - K_3K_2} \end{aligned}. \tag{II.1.31}$$

Based on (II.1.31), the contact pressures on all the other rotor surfaces can be determined by (II.1.20). Subsequently, tangential and radial stresses on each layer can be achieved based on TABLE II and, thus, the Von Mises equivalent stress can be computed in accordance with (II.1.19).

In conclusion, apart from contact pressures and Von Mises equivalent stress, another aspect that has to be considered in designing the HS-PMSM rotor consists of its critical speeds. These represent the natural speeds of the rotor, in correspondence of which resonance phenomena would occur, thus leading to rotor failure. Therefore, the rotor first critical speed has to be considered, which should not be reached in order to preserve HS-PMSM rotor integrity. This value can be estimated as

$$\omega_{m,cr} = \sqrt{\frac{g}{d_{st}}} \tag{II.1.32}$$

in which g is gravity acceleration constant and d_{st} is the rotor static deflection, which depends on rotor layers geometry and different material properties [34].

II.2. Electromagnetic Modeling

The electromagnetic modelling has been developed by referring to the same HS-PMSM structure shown in Fig. 1, which has been redrawn appropriately in Fig. 5. This consists of an inner rotor made up of four cylindrical layers, namely rotor shaft, rotor back-iron, PMs and sleeve. Whereas the outer stator consists of two layers: iron teeth and slots, which host a distributed three-phase winding, and the stator back-iron. The layer between stator and rotor is the airgap.

Based on this HS-PMSM configuration, the equivalent airgap includes the sleeve as it has the same permeability of the air, so it acts as an additional airgap from a magnetic point of view. Consequently, since the drops of magnetomotive force (mmf) within all the iron paths are just a little percentage of the overall mmf drop due to the large equivalent airgap, these contributions can be neglected safely. This assumption is corroborated also by the fact that no magnetic saturation phenomena is foreseen due to the relatively low magnetic flux density required by the HS-PMSM.

Furthermore, magnetic flux density is assumed characterized by radial component only; although this assumption may not be completely valid in presence of large equivalent airgap, it enables the achievement of a simple electromagnetic model, whose preliminary results can be refined during a second design stage through suitable Finite Element Analysis (FEA).

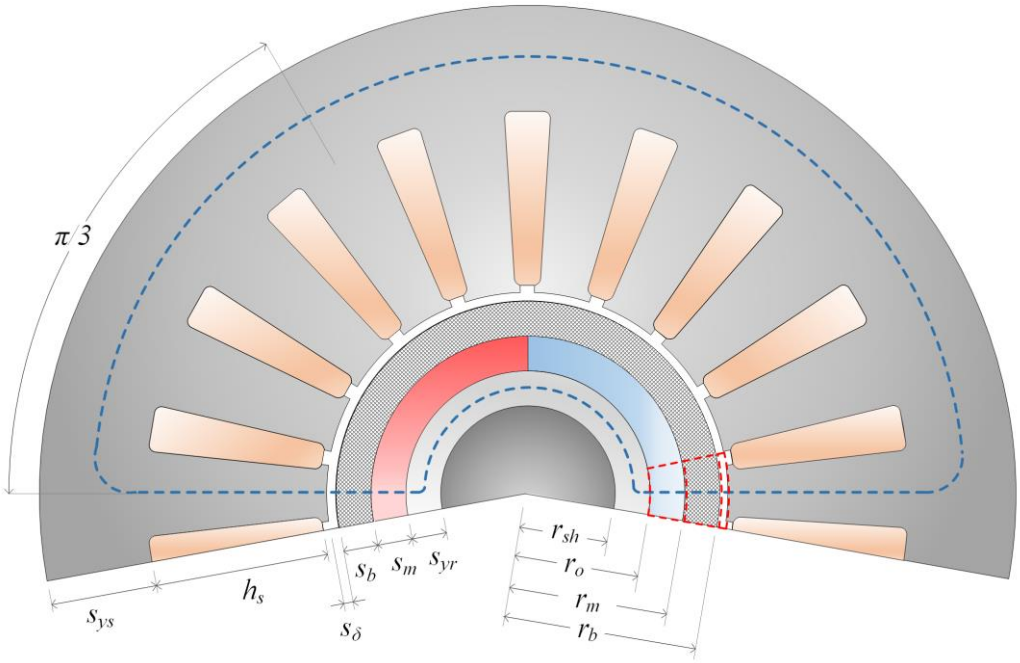

Fig. 5 HS-PMSM structure: main magnetic flux path (blue) and surfaces (red) considered for applying the Ampère's and Gauss' Laws.

Therefore, considering the application of the Ampère's Law to the closed magnetic flux path depicted in blue in Fig. 5, the following equation can be deduced:

$$2\int_0^{s_m}\left(\frac{B_m}{\mu_m}+H_c\right)ds+2\int_0^{s_b}\frac{B_b}{\mu_0}ds+2\int_0^{s_\delta}\frac{B_\delta}{\mu_0}ds=n\cdot I_{eq} \qquad \text{(II.2.1)}$$

where B_m, B_b and B_δ are the magnetic flux densities within PMs, sleeve and air gap respectively, whereas μ_m is the PM magnetic permeability and H_c is the PM coercive force. Moreover, I_{eq} and n are the equivalent current and the number of turns of a generic phase winding, whose product is thus the overall stator mmf. Subsequently, the Gauss' Law is applied to the closed surfaces red-highlighted in Fig. 5, which envelope the separation surfaces between rotor yoke and PMs, PMs and sleeve, and sleeve and air gap. Hence, still assuming the magnetic flux density characterized by the radial component only and that it is square-shaped, the following relationship holds:

$$B(s)\cdot(r+s)=B(0)\cdot r \quad , \quad s\geq 0\,. \qquad \text{(II.2.2)}$$

Therefore, considering each rotor layer, (II.2.3)-(II.2.5) can be achieved:

$$B_m(s) = B_0^{(m)} \frac{r_o}{r_o + s} \quad , \quad s \in [0, s_m] \tag{II.2.3}$$

$$B_b(s) = B_0^{(m)} \frac{r_o}{r_o + s_m + s} \quad , \quad s \in [0, s_b] \tag{II.2.4}$$

$$B_\delta(s) = B_0^{(m)} \frac{r_o}{r_o + s_m + s_b + s} \quad , \quad s \in [0, s_\delta] \tag{II.2.5}$$

where $B_m^{(0)}$ is the magnetic flux density on the contact surface between PMs and the rotor yoke. While s_m, s_b and s_δ denote the thickness of PM ring, sleeve and airgap respectively. Therefore, by substituting (II.2.3)-(II.2.5) in (II.2.1), the following result is achieved:

$$B_0^{(m)} \left[\frac{r_o}{\mu_m} \ln\left(1 + \frac{s_m}{r_o}\right) + \frac{r_o}{\mu_0} \ln\left(1 + \frac{s_b + s_\delta}{r_o + s_m}\right) \right] + s_m H_c = \frac{n I_{eq}}{2} . \tag{II.2.6}$$

Based on (II.2.6) and considering no magnetic saturation phenomena occurring, the principle of superimposition can be applied in order to identify the contributions of PMs and stator mmf to the overall magnetic flux density. First of all, it is possible to express (II.2.6) as

$$\frac{B_0^{(m)}}{\mu_0} r_{eq} + H_c s_m = \frac{n I_{eq}}{2} \tag{II.2.7}$$

where r_{eq} is defined as

$$r_{eq} = r_o \left(\frac{\mu_0}{\mu_m} \ln\left(1 + \frac{s_m}{r_o}\right) + \ln\left(1 + \frac{s_b + s_\delta}{r_o + s_m}\right) \right) . \tag{II.2.8}$$

Hence, based on (II.2.7), it is possible to identify the contributions of PMs ($B_{0,m}^{(m)}$) and stator mmf ($B_{0,i}^{(m)}$) by nullifying I_{eq} and H_c respectively, leading to

$$B_{0,m}^{(m)} = -\mu_0 H_c \frac{s_m}{r_{eq}} , \quad B_{0,i}^{(m)} = \mu_0 \frac{n I_{eq}}{2 r_{eq}} . \tag{II.2.9}$$

Therefore, it is possible to define a suitable relationship between these two magnetic flux densities as

$$\alpha = \frac{B_{0,i}^{(m)}}{B_{0,m}^{(m)}} \tag{II.2.10}$$

where α is defined as the magnetic ratio, which has to be chosen within (0,1) carefully in order to prevent PM demagnetization, but also to guarantee the capability to operate above the rated speed (flux-weakening operation). In this regard, it is worth noting that low values of α imply low magnetic flux density generated by the stator mmf and, thus, no PM demagnetization issues. However, these low values also prevent adequate flux-weakening capability and, thus, wide operating speed range. Consequently, α should be chosen as high as possible in accordance with desired rated and maximum speeds until this does not imply PM demagnetization. By substituting (II.2.9) in (II.2.10), the relationship between s_m, H_c and I_{eq} is achieved as

$$n \cdot I_{eq} = -\alpha \cdot 2H_c \, s_m \, . \tag{II.2.11}$$

Based on (II.2.11), it is possible to determine the PM thickness in accordance with H_c and I_{eq} for a desired α value: the former (H_c) depends on the chosen PM material, while I_{eq} is proportional to HS-PMSM torque and power capability.

Since square-shaped magnetic flux density has been assumed, the HS-PMSM is designed with trapezoidal back-electromotive forces (emfs) by assuming each phase winding distributed uniformly over an angular sector of $\pi/3$ per pole. This is done in order to enable Brushless DC operation (BLDC), by means of which higher torque density and/or reduced Joule losses can be achieved compared to Brushless AC solutions, as further detailed in the next chapter. Therefore, the rated electromagnetic power of the proposed HS-PMSM configuration can be determined as

$$P_n = 2 \cdot E_n \cdot I_n \tag{II.2.12}$$

where rated back-emf magnitude (E_n) and phase current magnitude (I_n) can be further expressed respectively as

$$E_n = \Lambda \cdot p \cdot \omega_{m,n} \quad , \quad I_n = \frac{I_{eq}}{2} \tag{II.2.13}$$

in which p denotes the number of pole pairs and $\omega_{m,n}$ is the rated speed, whereas Λ is the magnetic flux linkage due to PMs only. The latter can be computed as

$$\Lambda = 2 \cdot n \cdot l_i \cdot r_o \cdot B_0^{(m)} \tag{II.2.14}$$

in which r_o denotes the inner PM radius and l_i is the machine active axial length. Therefore, the substitution of both (II.2.13) and (II.2.14) in (II.2.12) yields

$$P_n = 2 \cdot p \cdot \omega_m \cdot n \cdot I_{eq} \cdot r_o \cdot l_i \cdot B_0^{(m)}. \tag{II.2.15}$$

As a result, by substituting the first equation of (II.2.9) in (II.2.15), the rated electromagnetic power becomes

$$P_n = -\mu_0 H_c s_m \frac{r_o}{r_{eq}} p\omega_{m,n} \cdot 2 l_i \cdot n I_{eq} \,. \tag{II.2.16}$$

Consequently, by combining (II.2.16) with (II.2.11), the following relationship is achieved:

$$P_n = 4\mu_0 \frac{r_o}{r_{eq}} p\omega_{m,n} \cdot l_i \cdot \alpha \cdot \left(H_c s_m\right)^2 \,. \tag{II.2.17}$$

In conclusion, based on (II.2.17), it is possible to define HS-PMSM main dimensions in accordance with design targets, such as P_n, $\omega_{m,n}$ and α, as well as with PM materials (H_c, μ_m). In this context, it is worth noting that all machine layer thicknesses should be chosen properly in order to assure PM retention at any speed and temperature within their corresponding operating ranges.

II.3. Analytical multi-parameter design procedure

II.3.1. Design targets and constraints

Based on both the mechanical and electromagnetic modelling introduced in the previous sections, it is possible to carry out the design of the HS-PMSM by introducing appropriate targets and constraints. The design targets are resumed in TABLE III, which have been defined considering a light duty electric vehicle. In particular, the rated power of the HS-PMSM has been chosen equal to 40 kW, slightly less than a Volkswagen Polo [35]. While the rated speed has been set to 30 krpm with the aim of limiting the motor size, considering also the employment of a magnetic gear as the vehicle transmission system [18]. Consequently, the rated torque should be equal to about 12.7 Nm. In addition, in order to be suitable for an automotive application, a wide constant-power speed range is foreseen. Hence, the maximum speed ($\omega_{m,max}$) is set to 100 krpm as a design target.

Regarding electromagnetic aspects, the coefficient α has been set to 0.7. This entails that stator rated current would reduce PM magnetic flux density down to 30% at most; this would prevent PM demagnetization issues at any speed, ensuring good flux-weakening capability at the same time. Due to the high-speed operation, the number of magnetic poles has been set to the lowest possible value, namely only two poles have been considered. Regarding winding configuration, a three-phase distributed winding

characterized by 3 slots per pole per phase has been chosen in order to assure a good trapezoidal shaped back-emfs. In addition, the number of turns of each phase winding has been determined by imposing a line-to-line back-emf magnitude lower than 400 V.

Apart from satisfying the design targets above mentioned, the HS-PMSM design must comply with several mechanical and electromagnetic constraints, which have to be satisfied at any operating condition. Regarding electromagnetic constraints, the desired α value must be achieved: this is of paramount importance when employing ferrite PMs, which are characterized by low coercive force and, thus, require limiting the rated stator current in order to prevent PM demagnetization at any operating condition. Consequently, based on (II.2.17), the following relationship has to be satisfied

$$\frac{r_{eq}}{r_o}\frac{P_n}{4\mu_0\, p\omega_{m,n}\cdot l_i\left(H_c s_m\right)^2}=\alpha^* \,. \tag{II.3.1}$$

Therefore, by substituting (II.2.8) in (II.3.1), the following relationship is achieved:

$$\alpha^*=\frac{\frac{r_o}{\mu_m}\ln\left(1+\frac{s_m}{r_o}\right)+\frac{r_o}{\mu_0}\ln\left(1+\frac{s_b+s_\delta}{r_o+s_m}\right)}{4\cdot p\cdot\omega_m\cdot l_i\cdot r_o\cdot\left(s_m\cdot H_c\right)^2}P_n \,. \tag{II.3.2}$$

Based on (II.3.2), it is possible to determine appropriate α-loci on the (s_m,l_i) plane that correspond to different α^* values, as depicted in Fig. 6. It can be seen that different combinations of s_m and l_i determine the same α^* value. Consequently, for a given α^* s_m and l_i have to be chosen in order to identify a point on (s_m,l_i) that lies on the corresponding α^* locus.

Once s_m and l_i have been chosen, n and I_n have to be determined accordingly. In particular, n can be easily calculated by imposing the desired line-to-line back emfs at rated speed as

$$E_n \le E_{n,max} \tag{II.3.3}$$

TABLE III HS-PMSM DESIGN TARGETS

Description	**Symbol**	**Unit**	**Value**
Rated power	P_n	kW	40
Rated speed	$\omega_{m,n}$	krpm	30
Maximum speed	$\omega_{m,max}$	krpm	100
Maximum Line-to-line voltage	$2E_{n.max}$	V	400
Rated torque	T_e	Nm	12.7
Magnetic ratio	α^*	[-]	0.70
Pole pairs	p	[-]	1

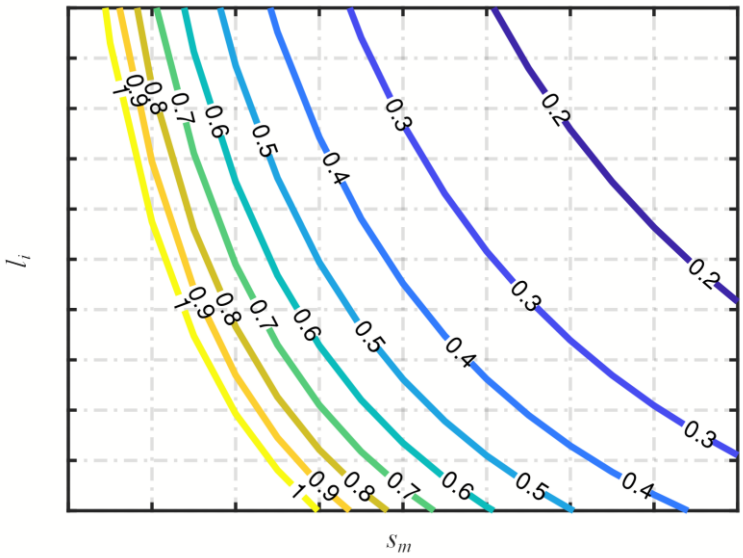

Fig. 6 An example of the α-loci on the (s_m,l_i) plane (each curve corresponds to the α^* value labelled on).

Therefore, based on (II.2.11) thorough (II.2.13), the following relationship is achieved:

$$n \le -\frac{2E_{n,\max} \cdot \alpha^* \left(s_m \cdot H_c \right)}{2P_n} \tag{II.3.4}$$

Consequently, n can be chosen as the highest natural number that complies with (II.3.4). Once n has been defined, the value of the rated current can be computed in accordance with the following relationship, which is obtained by substituting (II.2.13) in (II.2.11):

$$I_n = -\frac{\alpha^* \cdot H_c \, s_m}{n}. \tag{II.3.5}$$

Furthermore. the most appropriate DC-link voltage value has to be chosen in order to satisfy the following constraint:

$$2E_n \le \gamma V_{dc} \tag{II.3.6}$$

in which V_{dc} is the DC-link voltage and γ is an a-dimensional coefficient, which should be imposed less than one in order to account for additional voltage drops and HS-PMSM controllability at any speed [36]. In particular, despite of trapezoidal-shaped emfs, a "three-phase-on" (3PO) control strategy is foreseen for the proposed HS-PMSM, which presents superior performances compared to conventional current commutation controls [28]. However, 3PO determines additional inductive voltage drops at steady state

operation, which can be roughly estimated in accordance with (II.2.10) as about α times the back-emfs due to PMs only. Therefore, assuming that these voltage drops occur on the quadrature axis compared to the back-emfs due to PM only, γ can be chosen in accordance with the following inequality:

$$\gamma \leq \frac{1}{\sqrt{1+\left(\alpha^{*}\right)^{2}}}. \tag{II.3.7}$$

Focusing now on sleeve design, minimum PM contact pressure and maximum Von Mises equivalent stress must be considered. In particular, rotor design must ensure PM retention at any operating condition, leading to

$$p_i^{(L2)} > 0\,. \tag{II.3.8}$$

Furthermore, in order to avoid mechanical failure, the Von Mises equivalent stress on the inner surface of the sleeve must be lower than its maximum allowable value (σ_{max}):

$$\sigma_{eq}^{(L3)} < \sigma_{max}^{(L3)}\,. \tag{II.3.9}$$

In conclusion, in order to avoid resonance phenomena, the critical speed must be reasonably higher than the HS-PMSM maximum speed. This is because HS-PMSM has to be mechanically capable to reach an overspeed at least 10% more than the maximum operating speed [37], [38] or even up to 20% [31]. Consequently, the following relationship has to be considered:

$$\omega_{m,cr} \gg \omega_{m,\max}\,. \tag{II.3.10}$$

II.3.2. Proposed design procedure

The design of the HS-PMSM described in this dissertation accounts for both mechanical and electromagnetic aspects; this task is not trivial for the analytical calculation because of the large number of parameters involved. In addition, many of them affect both mechanical and electromagnetic aspects, which cannot be thus managed separately. Consequently, a fast and analytical multi-parameter design procedure has been developed in order to achieve a suitable preliminary HS-PMSM design by optimizing a given cost function.

The proposed procedure starts from a large HS-PMSM "population", namely a number of HS-PMSM configurations have been considered. In particular, each HS-PMSM configuration is represented by a multi-parameter array (x), which consists of both

tuneable and derived parameters, as pointed out in TABLE IV. The tuneable parameters vary independently from each other within appropriate ranges and by appropriate steps. Whereas derived parameters are calculated from the tuneable ones in accordance with mechanical and/or electromagnetic models introduced in the previous sections.

The procedure firstly rejects all the HS-PMSM configurations that do not comply with the design constraints, while it passes all the others. As a result, an allowable set of HS-PMSM configurations is determined (X), as highlighted in Fig. 7. Hence, in order to identify a specific HS-PMSM configuration among all those belonging to X, an optimization criterion must be defined. Considering the application for which the HS-PMSM is designed (automotive), many optimization criteria can be used, such as the minimum HS-PMSM volume, the minimum axial length, the minimum sleeve and/or PM thicknesses. For example, minimizing the sleeve thickness could be the best idea in order to allow better PM cooling and reducing the equivalent airgap. On the other hand, minimizing the active volume or the active length could allow the HS-PMSM to be employed where small sizes are the strictest requirement. Therefore, a general optimization criterion can be introduced as

$$x = x^* \,, \quad f(x^*) = \min_{x \in X} \left\{ f(x) \right\} \tag{II.3.11}$$

where f can be chosen differently in order to optimize different HS-PMSM properties, such as the minimum volume, minimum axial length, minimum sleeve or PM thickness.

TABLE IV HS-PMSM CONFIGURATION PARAMETERS

	Parameters	**Symbol**	**Unit**
Tuneable	Outer PM radius	r_m	mm
	PM thickness	s_m	mm
	Sleeve thickness	s_b	mm
	Sleeve interference fit	δ	mm
	Active machine axial length	l_i	mm
Derived	Sleeve tensile strength	$\sigma_{eq}^{(Ls)}$	MPa
	PM contact pressure	$p_o^{(L1)}$	MPa
	Rotor critical speed	ω_{cr}	krpm
	Magnetic ratio	α	-
	Rated current	I_n	A
	Number of turns per phase	n	turns

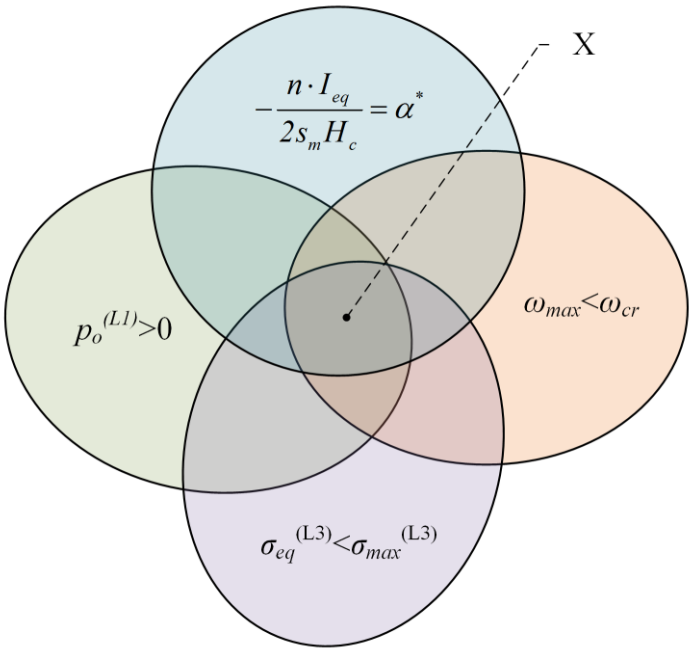

Fig. 7 Allowable set of multi-parameter arrays (X) determined by the proposed design procedure.

II.4. Analytical results and Finite Element Analyses

The proposed analytical multi-parameter design procedure has been implemented for designing a number of HS-PMSMs with the aim of identifying the most suitable configuration for the specific application (traction motor of a light duty electric vehicle). For each HS-PMSM configuration, Finite Element Analyses (FEAs) have been carried out by means of Solidworks and JMAG. This is done in order to corroborate the effectiveness of the proposed design procedure, but also with the aim of investigating HS-PMSM performances not covered by the analytical procedure due to modelling issues, such as magnetic flux density distribution within rotor and stator frames. The FEA simulations carried out with SolidWorks regard the mechanical forces acting on the sleeve and on the PMs, i.e. the σ_{eq} and p_o space distributions, as well as the evaluation of the critical speed by means of special functions of the SolidWorks software. While JMAG Designer has been used in order to assess electromagnetic performances of the designed HS-PMSMs, especially in terms of magnetic flux density distribution, back-emf and cogging torque evolutions at different HS-PMSM operating conditions.

II.4.1. Preliminary results: sleeve and PM materials evaluation

Analytical and FEA results firstly regard the use of different sleeve and PM materials, whose main properties are reported in TABLE V. Regarding sleeve materials, Titanium

and Carbon Fiber Reinforced Polymer (CFRP) have been considered alternatively; Titanium presents high specific mass density (ρ_s) and low maximum stress ($\sigma_{s,max}$) compared to CFRP. The latter is characterized also by a slightly negative thermal expansion coefficient, which may be suitable at high temperature operation. Similarly, to sleeve materials, NdFeB and Ferrite PMs have been considered alternatively for comparison purposes: NdFeB presents very high coercive force and residual magnetism compared to ferrite PMs, as well as a lower thermal expansion coefficient. In this regard, maximum temperature variations (ΔT_{max}) are imposed equal to 60 °C and 120 °C for NdFeB-based and Ferrite-based HS-PMSM respectively in order to take into account different PM thermal properties. This is because NdFeB suffers from reduced maximum operating temperature and greater specific mass density compared to ferrite PMs.

Apart from PM and sleeve materials, some other HS-PMSM parameters have been imposed; the mechanical airgap s_δ is imposed equal to 1.5 mm in order to allow the relative motion between stator and rotor, even in case of small rotor deformations at the maximum operating speed. While the DC-link voltage and γ have been set to 560 V and 0.7 respectively. In conclusion, regarding stator and rotor back-iron, the VACOFLUX 48 material has been selected, which exhibits very good electromagnetic properties [39].

Regarding stator windings, litz wires have been considered because they are particularly recommended for high-speed electrical machines [40]–[42]. Therefore, a maximum current of 0.15 A is imposed for each strand (AWG30), leading to an overall current density of about 3 A/mm^2. The geometrical slot fill factor has been imposed equal to 0.54, which is the same value of the ratio between slot and tooth widths.

Then, slot sizes have been calculated. Finally, stator yoke width has been determined in order to achieve fair values of magnetic flux density, by taking into account also the necessity to minimize iron losses at high-speed operation.

TABLE V SLEEVE AND PM MATERIAL PROPERTIES

Description	**Symbol**	**Unit**	**Value**	
Sleeve			***CFRP 60%***	***Titanium***
Specific mass density	ρ_s	kg/m^3	1500	4500
Young's modulus	E_Y	GPa	240	120
Poisson's ratio	υ	[-]	0.30	0.34
Maximum stress	$\sigma_{s,max}$	GPa	2.4	1.2
Permanent Magnets			***Ferrite***	***NdFeB***
Specific mass density	ρ_m	kg/m^3	5100	7500
Coercive force	H_c	A/m	330000	1015000
Residual magnetism	-	T	0.435	1.37

Two HS-PMSMs have been designed at first by imposing a maximum speed of 60 krpm, the corresponding main parameters being summarized in TABLE VI. Only Titanium sleeves have been considered in this case because the Titanium maximum stress is high enough in order to comply with the imposed maximum operating speed. The comparison between NdFeB-based and Ferrite-based solutions reveals significant differences occurring on PM and sleeve thicknesses, as expected. In particular, NdFeB PMs are very thin compared to Ferrite PMs, thus requiring a thinner sleeve too. The volume of NdFeB PMs is also significantly lower than Ferrite PMs. As a result, the employment of high-energy density PMs leads to a smaller and significantly shorter HS-PMSM configuration, as highlighted in TABLE VI. Referring now to the Von Mises equivalent stress and PM contact pressure, their evolutions with some of the main HS-PMSM design parameters are shown in Fig. 8. For each design parameter, the evolutions of $\sigma_{eq}^{(L3)}$ and $p_o^{(L1)}$ are considered by assuming all the other parameters constant and equal to those shown in TABLE VI. Focusing on rotor outer radius at first, it can be seen that larger radii lead to lower stress for both configurations, but these reduce PM contact pressure as well. Furthermore, although a larger PM volume has to be hosted by Ferrite-based rotor, its outer radius is very similar to NdFeB-based rotor. Different considerations can be made for sleeve thicknesses, which differ significantly from each other. This is mainly due to large Ferrite PM thickness, which is four times that of NdFeB-based configuration. Regarding interference fit, the corresponding stress evolutions are almost superimposed for both PM materials. Whereas PM contact pressures differ significantly due to rotor structure and material properties. Consequently, since PM contact pressure benefits from a high interference value, this is maximized in both cases unless it does not comply with the maximum allowable value of the Von Mises equivalent stress. This results in the same interference value for both NdFeB-based and Ferrite-based HS-PMSM configurations. In conclusion, Fig. 8 highlights also that the Von Mises equivalent stress increases with rotor speed, the opposite occurring for PM contact pressure, as expected. In particular, maximum operating speed is bounded by PM contact pressure issues rather than by stress constraint.

Subsequently, another HS-PMSM design has been carried out by referring to a maximum speed of 100 krpm, whose corresponding analytical results are reported in TABLE VII. In this case, Titanium has been replaced by CFRP because the former is not able to guarantee PM retention at this maximum operating speed, as detectable by comparing Fig. 8 to Fig. 9. The latter reveals a significant increase of $\sigma_{eq}^{(L3)}$ that cannot be fulfilled by any Titanium sleeve.

TABLE VI HS-PMSM PARAMETERS AND RATED VALUES (TITANIUM SLEEVE)

Description	Symbol	Unit	NdFeB-based	Ferrite-based
Maximum speed	$\omega_{m,max}$	krpm	60	60
Rated current	I_n	A	99.2	99.2
Phase resistance	R	mΩ	9.2	15.8
Phase inductance	L	mH	47.0	78.5
Shaft radius	r_{sh}	mm	12.5	12.5
Rotor yoke thickness	s_{yr}	mm	22	13.5
PM thickness	s_m	mm	2.5	10
Sleeve thickness	s_b	mm	1.5	5.5
Interference fit	δ	mm	0.25	0.25
Stator outer radius	r_s	mm	119.9	136.2
Stator back-iron	s_{ys}	mm	30.5	34.6
Slot height	h_s	mm	46.5	55.6
Active length	l_i	mm	80	157
Active volume	V_a	cm^3	3613	9324
Magnet volume	V_{PM}	cm^3	44.9	311.6

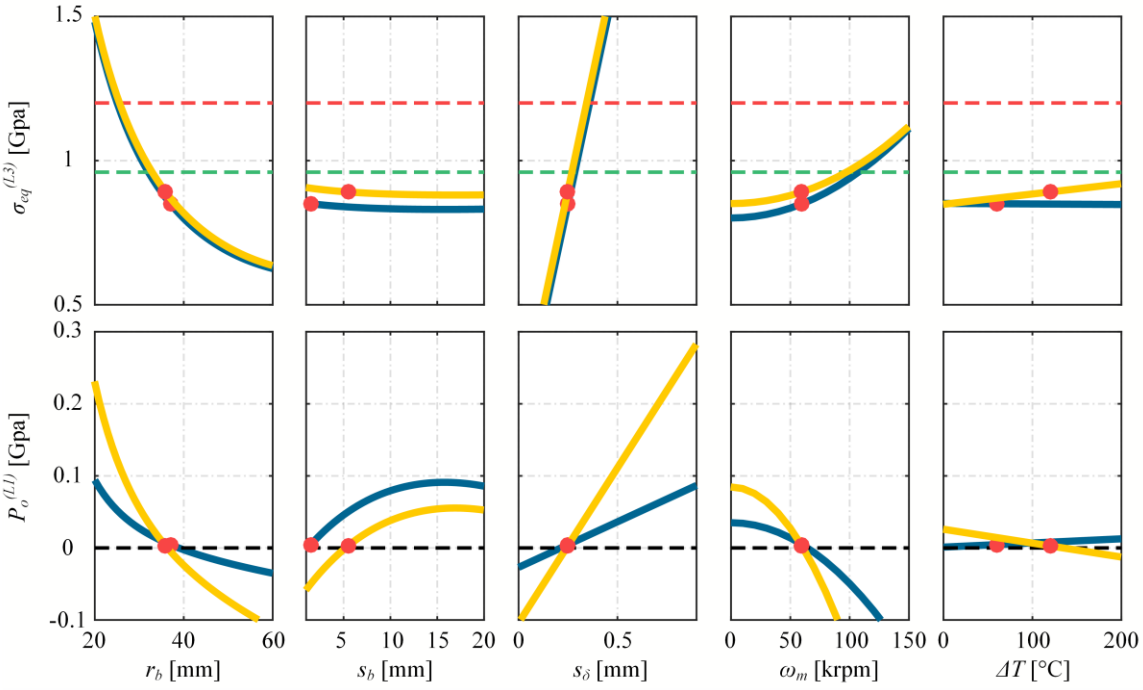

Fig. 8 The Von Mises equivalent stress on Titanium sleeves (top) and PM contact pressure on inner PM surface (bottom) as a function of main design parameters: NdFeB-based (blue) and Ferrite-based (yellow) HS-PMSM. The red dots highlight the designed configurations.

TABLE VII HS-PMSM PARAMETERS AND RATED VALUES (CFRP SLEEVE)

Description	Symbol	Unit	NdFeB-based	Ferrite-based
Maximum speed	$\omega_{m,max}$	krpm	100	100
Rated current	I_n	A	99.7	98.7
Phase resistance	R	mΩ	9.3	15.9
Phase inductance	L	mH	49.6	82.7
Shaft radius	r_{sh}	mm	12.5	12.5
Rotor yoke thickness	s_{yr}	mm	17	11.5
PM thickness	s_m	mm	2.5	10
Sleeve thickness	s_b	mm	1.5	5
Interference fit	δ	mm	0.2	0.2
Stator outer radius	r_s	mm	116.9	134.7
Stator back-iron	s_{ys}	mm	29.7	34.2
Slot height	h_s	mm	49.2	57
Active length	l_i	mm	92	167
Active volume	V_a	cm^3	3947	9521
Magnet volume	V_{PM}	cm^3	44.4	304.3

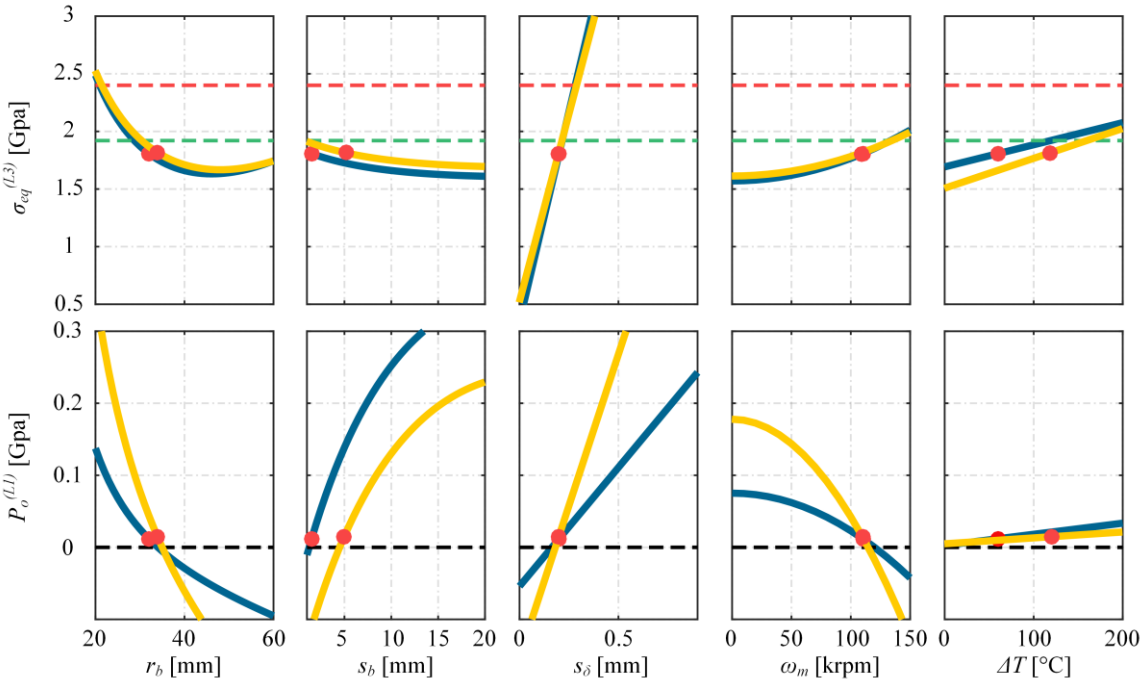

Fig. 9 The Von Mises equivalent stress on CFRP sleeves (top) and PM contact pressure on inner PM surface (bottom) as a function of main design parameters: NdFeB-based (blue) and Ferrite-based (yellow) HS-PMSM. The red dots highlight the designed configurations.

Consequently, CFRP has to be employed due to its higher maximum allowable stress, which is almost double compared to Titanium. The comparison between CFRP-based and Titanium-based solutions also reveals increased HS-PMSM active volumes, especially for the NdFeB-based solution, smaller differences occurring on all the other machine parameters.

The analytical results achieved for both Titanium-based and CFRP-based HS-PMSMs have been validated through an extensive FEA, which has been carried out by means of both JMAG and SolidWorks. In particular, JMAG has been used in order to assess electromagnetic performances of the designed HS-PMSM configurations, especially in terms of magnetic flux density distribution, back-emf and torque evolutions. Whereas mechanical stresses on the HS-PMSM rotor have been investigated by means of SolidWorks, which enables the computation of contact pressures and the Von Mises equivalent stresses acting on each rotor layer.

First of all, FEA has regarded the two Titanium-based HS-PMSMs and the corresponding results are shown from Fig. 10 to Fig. 12. In particular, both contact pressure and Von Mises equivalent stress have been evaluated at the worst operating conditions in terms of both speed and temperature. In this context, it is worth noting that NdFeB-based configuration benefits from increased temperature due to the low thermal expansion coefficient of PMs compared to both Titanium sleeve and rotor back-iron. This does not occur in case of Ferrite PMs, which are characterized by a very large thermal coefficient. Consequently, in the latter case, the worst thermal operating conditions are those characterized by the maximum temperature. Referring to Fig. 10, it can be seen that the contact pressure is always positive within the PM layer and it reaches its maximum value on the contact surface between PMs and the sleeve. On the same surface, the Von Mises equivalent stress is maximum, but still below the Titanium maximum stress, as highlighted in Fig. 11. The very good agreement between analytical and FEA results is highlighted in Fig. 12. This reveals also higher PM contact pressure and Von Mises equivalent stress for the Ferrite-based configuration due to the higher PM thickness.

Subsequently, FEA has been focused on the two CFRP-based HS-PMSM configurations, which have been designed for a maximum speed of 100 krpm. The corresponding results are depicted from Fig. 13 to Fig. 15. They reveal higher equivalent stress and contact pressure compared to the Titanium-based cases, as expected. The most important differences consist also of the need of evaluating the Von Mises equivalent stress of NdFeB-based configuration at the maximum temperature, whereas PM contact pressure of Ferrite-based configuration has to be evaluated at the minimum operating temperature. These differences are due to the negative thermal expansion coefficient of CFRP, which increases both PM contact pressures and Von Mises equivalent stresses as

the temperature increases. Also in this case, a very good agreement between analytical and FEA results is achieved, revealing the effectiveness of the proposed analytical design procedure.

In conclusion, main analytical and FEA results are summarized in TABLE VIII and TABLE IX. It can be seen that magnetic flux densities achieved by FEA on the contact surfaces between rotor back-iron and PM ring are lower than those computed by the proposed analytical procedure. This may be due to the several assumptions imposed for carrying out the electromagnetic design. However, it is worth noting that the magnetic ratio α is quite similar in all cases, thus PM demagnetization is always prevented. Regarding rated power and torque, very similar results are achieved for the NdFeB configurations. This does not occur for Ferrite-based HS-PMSMs, namely rated power and torque computed by FEA are less than expected. This is due mainly to the un-ideal trapezoidal shapes of the back-emfs caused by the large equivalent airgap of the Ferrite-based configurations (6.5-7 mm), which accounts for both sleeve thickness (5-5.5 mm) and airgap (1.5 mm). Consequently, torque drops occur, even in presence of ideal current commutations, leading to reduced average torque and power capability. This unsuitable phenomenon does not occur in NdFeB-based configurations, which are characterized by much thinner sleeves (1.5 mm) and, thus, much thinner airgaps (just 3 mm).

II.4.2. Analytical and FEA results

Based on both analytical and FEA results shown and discussed in the previous section, the analytical multi-parameter design procedure is applied by considering CFRP sleeve and ferrite-based PMs only: the former is unavoidable in order to enable high speed operation (> 60 krpm), while Ferrite PMs have been preferred to NdFeB due to cost and price fluctuation issues [43].

Compared to the HS-PMSM configurations considered in the previous subsection, some other design parameters have been changed. First of all, although litz wires are particularly recommended for high-speed electrical machines [40]–[42], these are very expensive and, thus, unsuitable for the motor of full-electric or hybrid-electric vehicles, which should be as cheap as possible. For this reason, an alternative solution has been adopted, namely the use of standard wires by accepting to have some more losses due to skin and proximity effects. Thus, the size of the wires has been calculated considering a maximum current density of about 10 A/mm^2 and a geometrical slot fill factor of 0.4 in accordance with the most used technical solutions currently available. Regarding rotor and stator core, the VACOFLUX 48 has been replaced by a less expensive and more common silicon steel (M235-35A): the latter presents a higher resistivity, but it is lighter, as highlighted in TABLE X.

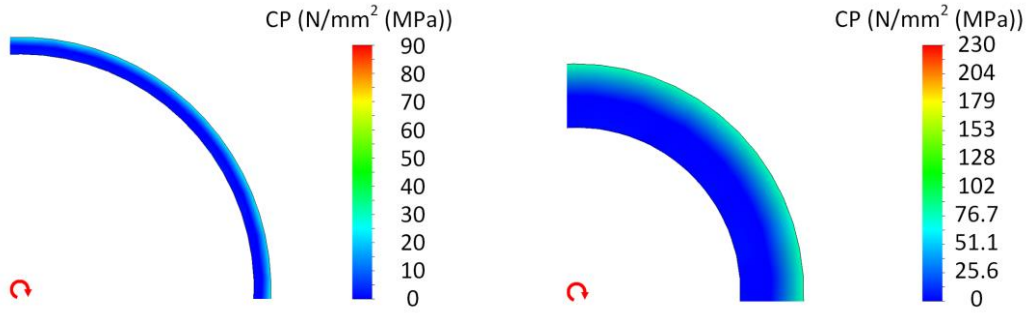

Fig. 10 PM contact pressures by employing a Titanium sleeve at 60 krpm: NdFeB-based (on the left, ΔT = 0 °C) and Ferrite-based configuration (on the right, ΔT = 120 °C).

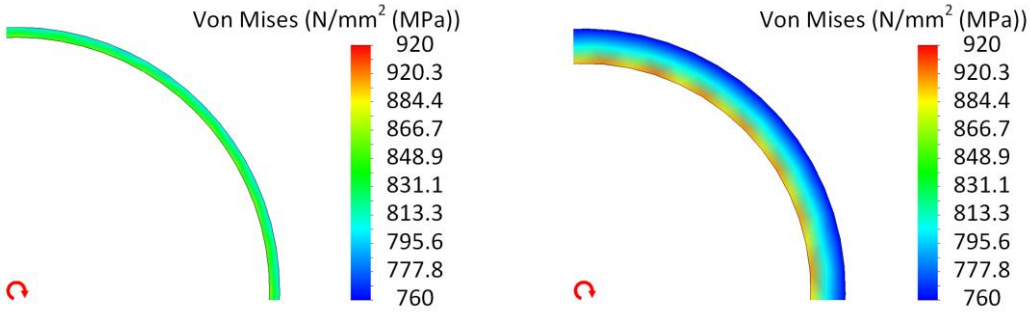

Fig. 11 The Von Mises equivalent stress on the Titanium sleeve at 60 krpm: NdFeB-based (on the left, ΔT = 0 °C) and Ferrite-based configuration (on the right, ΔT = 120 °C).

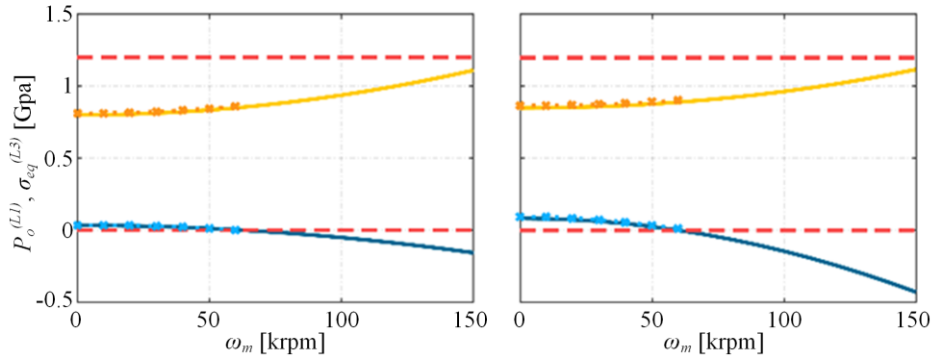

Fig. 12 Comparison of stresses and contact pressures achieved by analytical procedure (solid lines) and FEA (dot-dashed lines) on NdFeB-based (on the left) and on Ferrite-based configuration (on the right) equipped with a Titanium sleeve: $\sigma_{eq}^{(L3)}$ (yellow, orange) and $p_i^{(L2)}$ (blue, cyan).

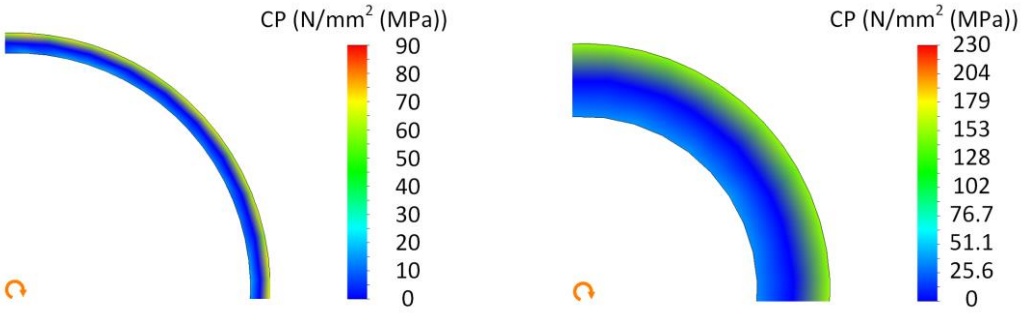

Fig. 13 PM contact pressures by employing a CFRP sleeve at 100 krpm: NdFeB-based (on the left, ΔT = 0 °C) and Ferrite-based configuration (on the right, ΔT = 0 °C).

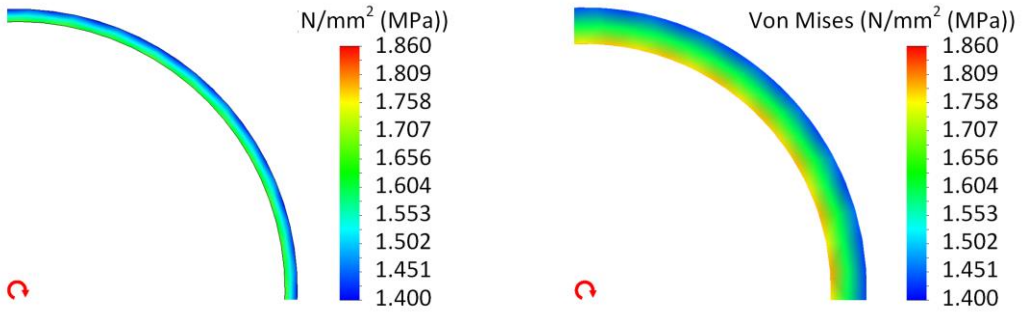

Fig. 14 The Von Mises equivalent stress by employing a CFRP sleeve at 100 krpm: NdFeB-based (on the left, ΔT = 60 °C) and Ferrite-based configuration (on the right, ΔT = 120 °C).

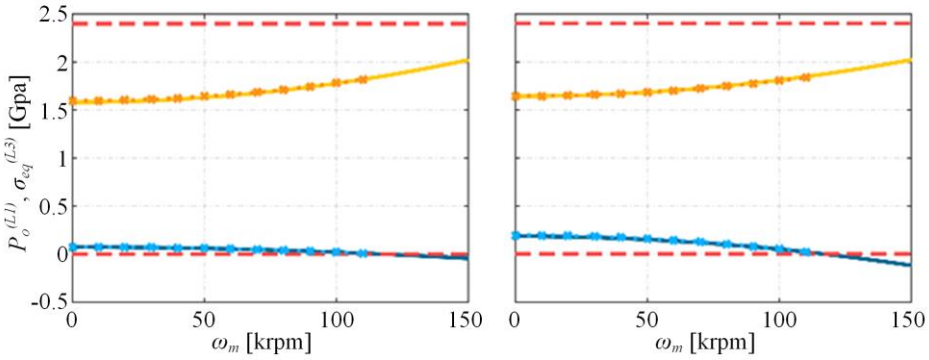

Fig. 15 Comparison of stresses and contact pressures achieved by analytical procedure (solid lines) and FEA (dot-dashed lines) on NdFeB-based (on the left) and on Ferrite-based configuration (on the right) equipped with a CFRP sleeve: $\sigma_{eq}^{(L3)}$ (yellow, orange) and $p_i^{(L2)}$ (blue, cyan).

TABLE VIII RESULT COMPARISON (TITANIUM SLEEVE @ 60 KRPM)

	Unit	NdFeB HS-PMSM		Ferrite HS-PMSM	
		Analytical	***FEA***	***Analytical***	***FEA***
P_n	kW	40	40.1 (+0.3%)	40	39.3 (-1.8%)
T_e	Nm	12.7	12.8 (+0.8%)	12.7	12.5 (-1.6%)
E	V	200.0	199.0 (-0.5%)	200.0	198.0 (-1.0%)
$B_o^{(m)}$	T	0.646	0.636 (-1.5%)	0.327	0.310 (-5.2%)
$B_o^{(i)}$	T	0.452	0.417 (-7.7%)	0.232	0.195 (-15.9%)
α	[-]	0.70	0.66 (-5.7%)	0.71	0.63 (-11.3%)
$\sigma_{eq}^{(L3)}$	MPa	851	856 (+0.6%)	890	893 (+0.3%)
$p_o^{(L1)}$	MPa	11.9	12.0 (+0.8%)	24.7	22.6 (-8.5%)

TABLE IX RESULT COMPARISON (CFRP SLEEVE @ 100 KRPM)

	Unit	NdFeB HS-PMSM		Ferrite HS-PMSM	
		Analytical	***FEA***	***Analytical***	***FEA***
P_n	kW	40	40.1 (+0.3%)	40	39.3 (-1.8%)
T_e	Nm	12.7	12.8 (+0.8%)	12.7	12.5 (-1.6%)
E	V	200.7	198.0 (-1.3%)	202.5	202.0 (-0.2%)
$B_o^{(m)}$	T	0.654	0.625 (-4.4%)	0.341	0.326 (-4.4%)
$B_o^{(i)}$	T	0.464	0.418 (-9.9%)	0.242	0.225 (-7.0%)
α	[-]	0.71	0.67 (-5.6%)	0.71	0.69 (-2.8%)
$\sigma_{eq}^{(L3)}$	MPa	1780	1782 (+0.1%)	1808	1801 (-0.4%)
$p_o^{(L1)}$	MPa	13.7	12.6 (-8.0%)	33.0	31.1 (-5.8%)

In addition, based on (II.3.7), γ has been reduced to 0.6 in order to enable a wider constant-power speed range, as well as for ensuring high HS-PMSM dynamic performances at any speed [5], [36]. The DC-link voltage has been thus imposed equal to 720 V in accordance with typical values occurring and foreseeing for electric vehicles [43], [44], as well as with HS-PMSM control needs.

Hence, five different optimization criteria have been chosen for comparison purposes, by means of which the minimization of active machine volume (MMV), PM thickness (MPT), PM volume (MPV), rated phase current magnitude (MCM) and active machine axial length (MML) is alternatively imposed. This leads to five different HS-PMSM, whose main parameters are summarized in TABLE XI.

TABLE X ROTOR/STATOR CORE MATERIAL PROPERTIES

Description	**Unit**	**Value**	**Value**
Rotor and Stator cores		***M235-35A***	***VACOFLUX 48***
Specific mass density	kg/m^3	7600	8120
Resistivity	μΩ·cm	59	42

TABLE XI HS-PMSM MAIN PARAMETERS

Description	**Symbol**	**Unit**	**MMV**	**MPT**	**MPV**	**MCM**	**MML**
Rated current	I_n	A	107.86	101.83	96.55	**96.08**	105.73
DC phase resistance	R	Ω	0.012	0.011	0.014	0.015	0.014
Shaft radius	r_{sh}	mm	12.5	12.5	12.5	12.5	12.5
Rotor yoke thickness	s_{yr}	mm	11.50	14.50	11.50	10.50	9.50
PM thickness	s_m	mm	11.0	**9.0**	11.0	11.0	12.0
PM volume	V_m	cm^3	289.5	292.1	**287.5**	321.1	295.6
Sleeve thickness	s_b	mm	5.0	4.0	5.0	7.5	6.5
Interference fit	δ	mm	0.25	0.25	0.25	0.20	0.20
Number of turns	n	turns	24	21	27	27	27
Stator outer radius	r_s	mm	193.5	185.7	200.9	203.3	201.7
Stator back-iron	s_{ys}	mm	24.6	23.6	25.5	25.8	25.6
Slot height	h_s	mm	28.2	25.3	31.0	30.4	30.8
Active length	l_i	mm	142	164	141	163	**140**
Active volume	V_{act}	cm^3	**4176**	4444	4472	5293	4475
Active weight	W_{act}	kg	31.4	33.6	33.9	39.6	33.6

The first configuration (MMV) is characterized by the minimum volume (4176 cm^3), as expected from the chosen optimization criterion. However, minimizing machine volume corresponds also to minimum machine weight; this is not generally true, but, in this case, it is due to similar densities of all the machine materials, as detectable in TABLE V and TABLE X. Moreover, it has to be specified that volume and weight do not account for the end-windings of the coils.

The second configuration (MPT) has been achieved by minimizing PM thickness; this leads also to the minimization of stator diameter and sleeve thickness, as still detectable in TABLE XI. Reduced sleeve thickness has been expected due to a lower maximum stress on the sleeve inner surface. Furthermore, from the electromagnetic point of view, both PM and sleeve thickness reduction leads to minimum equivalent air gap; this limits the dispersions of the magnetic flux density from the radial direction, making the preliminary assumption of considering only its radial component more consistent. The MPT is characterized also by the lowest DC phase resistance among all the considered

configurations, rated phase current being also reduced by about 5.6% compared to MMV. However, PM thickness minimization requires increased axial length compared to MMV (+15.5%) in order to comply with electromagnetic design targets, especially the rated torque. This leads to increased volume and weight, as still highlighted in TABLE XI.

The third configuration (MPV) does not show any particular advantages compared to the previous ones. It is very similar to MMV, except for rated phase current and slot height, which are reduced (–10.5%) and increased (+9.9%) respectively. A slightly lower rated phase current is achieved by the MCM (fourth configuration). However, this occurs at the cost of a significant increase of sleeve thickness (+50%), machine volume (+26.7%) and weight (+26.1%) compared to MMV. The last configuration (MML) presents the lowest axial length in accordance with the chosen optimization criterion. However, the axial length is only slightly lower than MMV (–1.5%), while PM and sleeve thickness are much greater (+9.1% and +30% respectively).

The comparison among all the considered configurations is resumed in the radar diagram shown in Fig. 16, in which all the parameters are reported in per unit with reference to those of the MMV configuration. The comparative analysis reveals that MMV, MPT and MML are comparable to each other, thus their choice depends on specific requirements and constraints.

The five HS-PMSM configurations analytically designed have been validated by FEAs from both electromagnetic and mechanical points of view. Considering the magnetic flux density distribution within rotor and stator frames shown in Fig. 17, this highlights a relatively low magnetic flux density without relevant saturation phenomena, as expected from the design stage. FEA simulations also refer to electromagnetic performances at

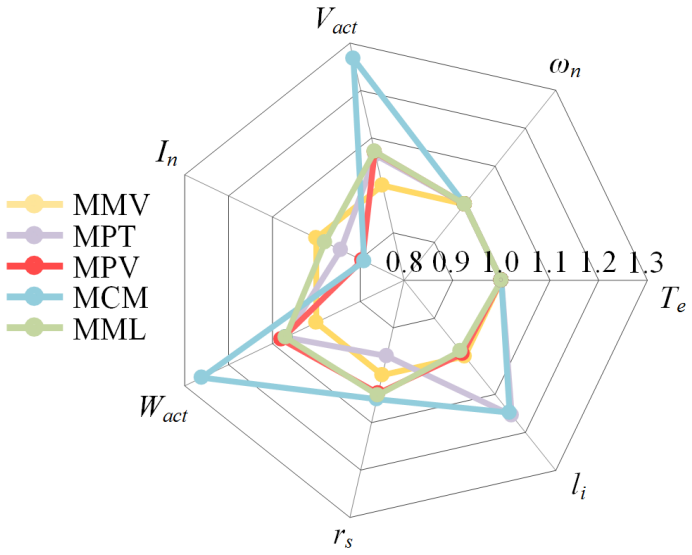

Fig. 16 Radar diagram of the five different HS-PMSM configurations (in pu with reference to MMV).

rated speed and torque, whose corresponding back-emf and torque evolutions are depicted in Fig. 18 and Fig. 19 respectively. Focusing on Fig. 18 at first, the back-emf shapes are almost trapezoidal for all the HS-PMSMs, although some differences occur. In particular, the phase back-emf magnitude are slightly greater for MPT and MCM, the lowest values being achieved for MMV and MML. In addition, almost linear evolutions are achieved for MCM and MML due to the large equivalent air gap. However, such a wide air gap "rounds" the edges of the back-emf shapes, making them less trapezoidal than in the other cases. Consequently, reduced average torque and significant torque ripple are achieved, as detectable from Fig. 19. This occurs because torque evolutions are determined by imposing the 3PO current profiles described in [28], which are computed assuming ideal trapezoidal-shaped back-emfs. However, both MCM and MML present very low cogging torque compared to the other configurations, as shown in Fig. 20.

The compliance of the designed HS-PMSMs with both mechanical and electromagnetic constraints is highlighted from Fig. 21 through Fig. 24. Considering the worst operating condition from a mechanical point of view (maximum speed), the values of $\sigma_{eq}^{(L3)}$ and $p_i^{(L2)}$ are within the allowable ranges. Considering now the magnetic flux density distribution achieved at rated and maximum speed (Fig. 23 and Fig. 24 respectively), the worst operating condition from an electromagnetic point of view occurs at the maximum speed because a significant demagnetizing current is required. However, Fig. 24 highlights that no PM demagnetization occurs for almost all the designed HS-PMSMs due to the appropriate choice of α^*, although some demagnetization issues may occur for MPV and, to a less extent, for MCM and MML. Whereas both MMV and MPT operate safely from this point of view.

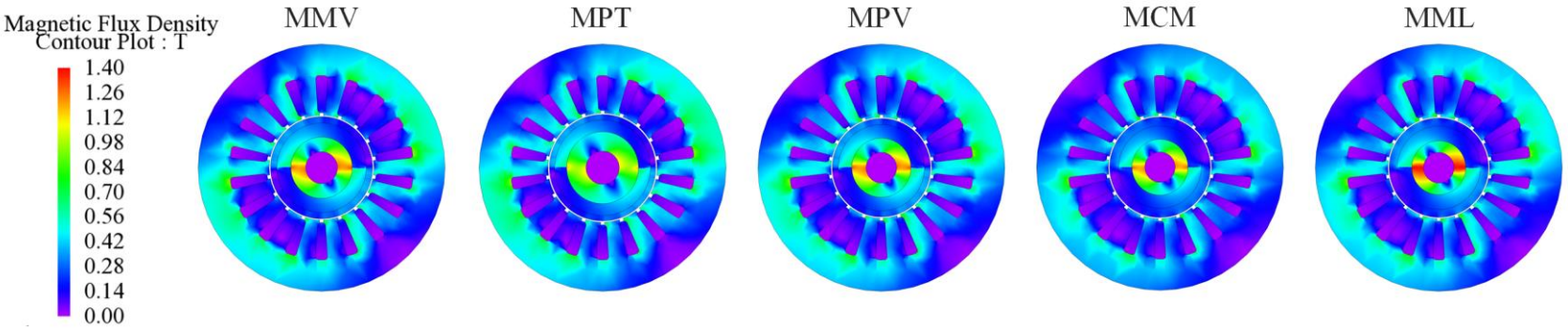

Fig. 17 Magnetic flux density distribution at rated speed and torque for the five HS-PMSMs.

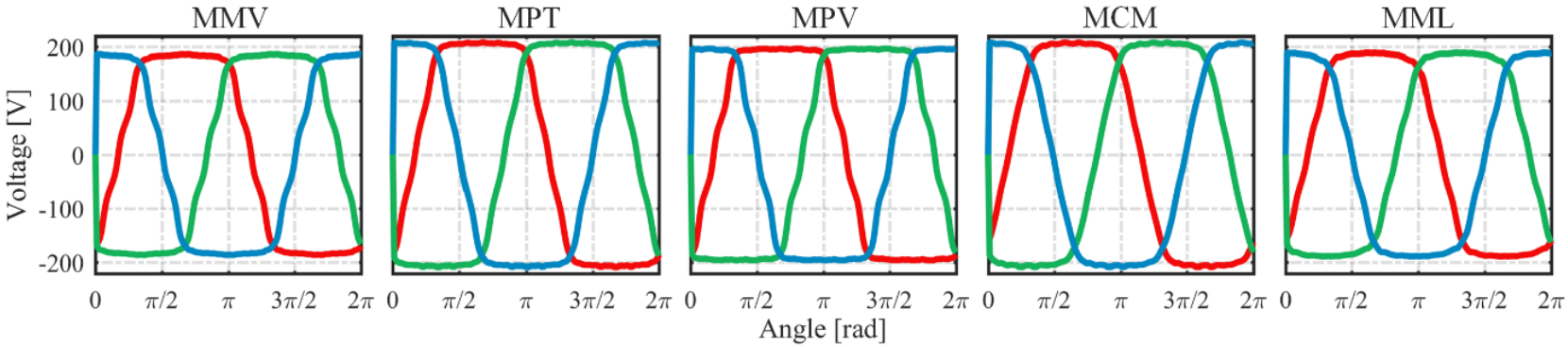

Fig. 18 Back-electromotive force achieved at the rated speed for the five HS-PMSMs through FEA simulations.

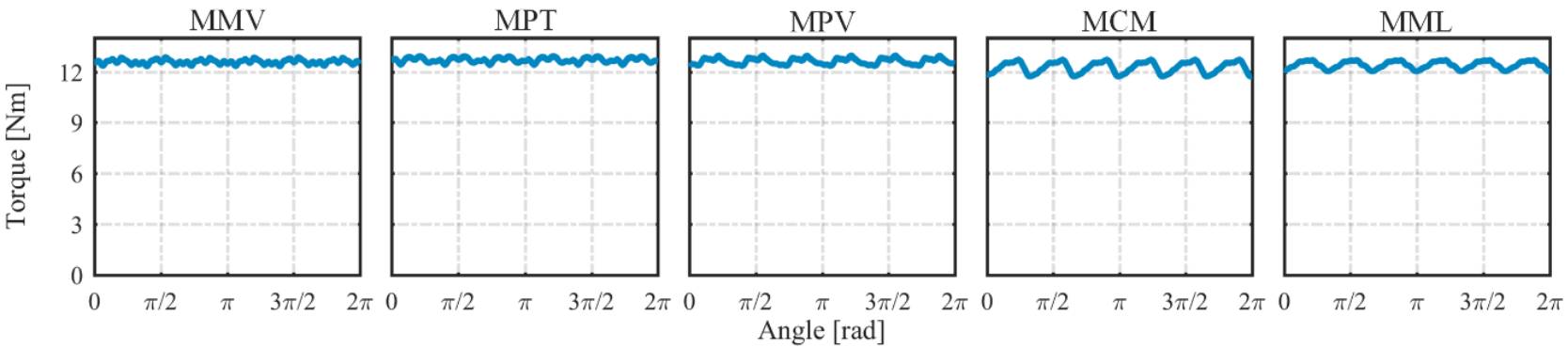

Fig. 19 Electromagnetic torque achieved at the rated speed for the five HS-PMSMs through FEA simulations.

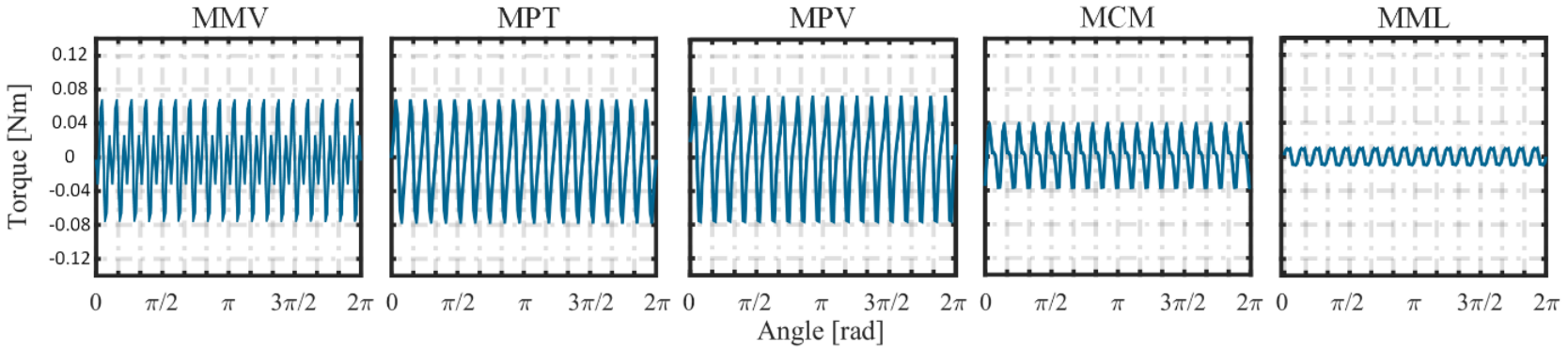

Fig. 20 Cogging torque achieved at the rated speed for the five HS-PMSMs through FEA simulations.

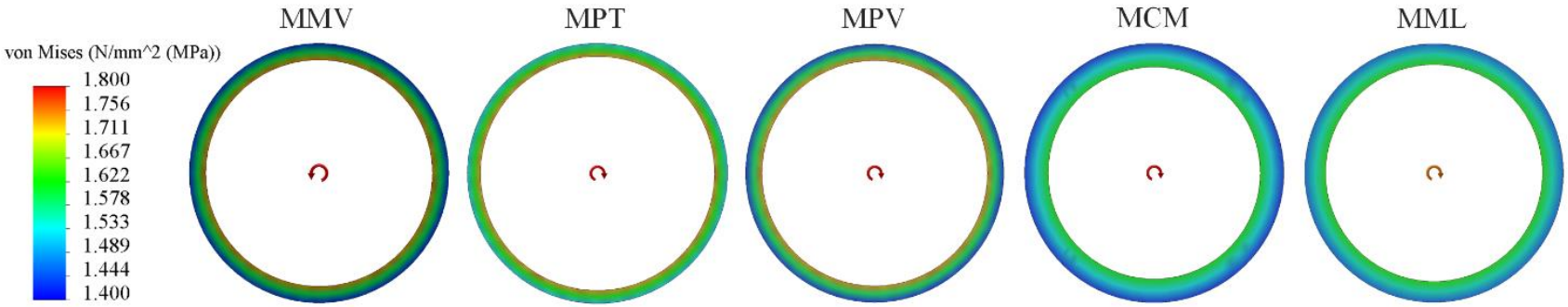

Fig. 21 Von Mises equivalent stress distribution in the CFRP sleeve at the maximum speed for the five HS-PMSMs.

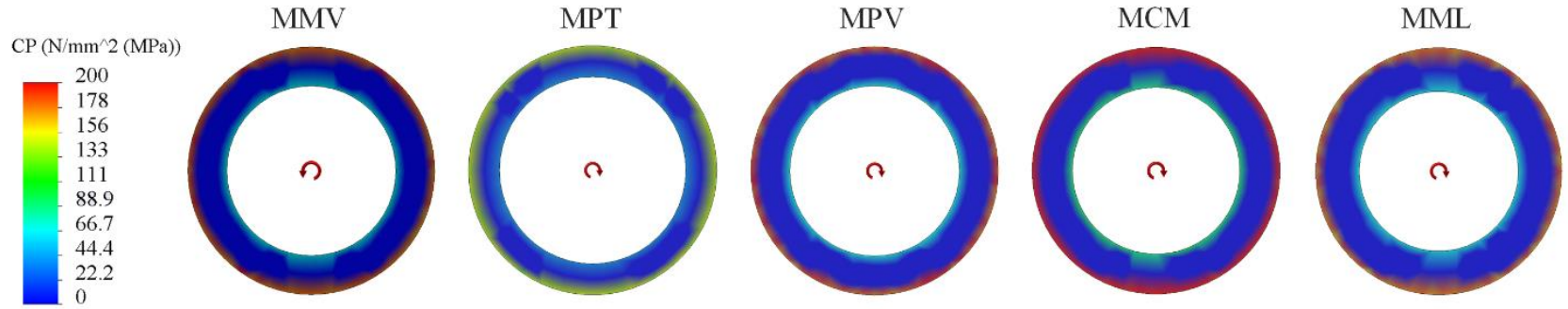

Fig. 22 Contact pressure in the ferrite PM at the maximum speed for the five HS-PMSMs.

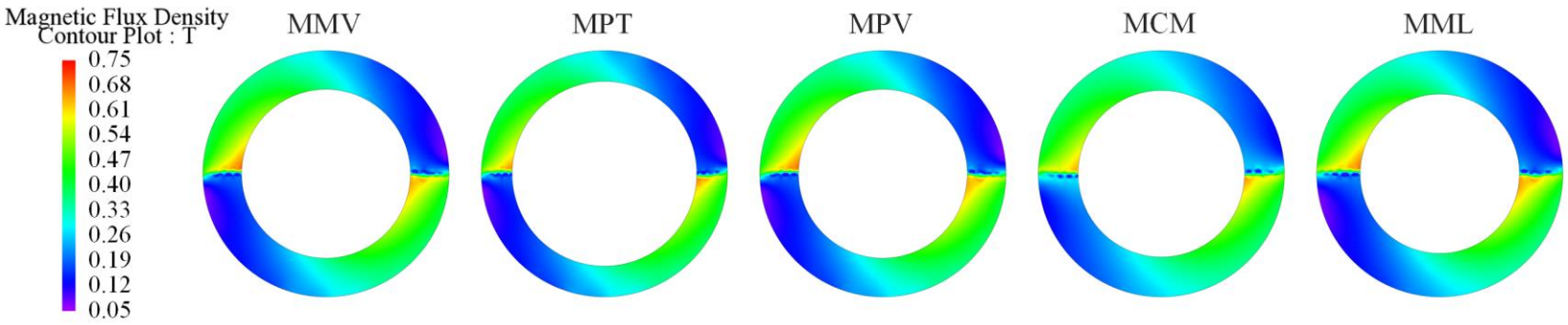

Fig. 23 Magnetic flux density distribution at the rated speed for the five HS-PMSMs.

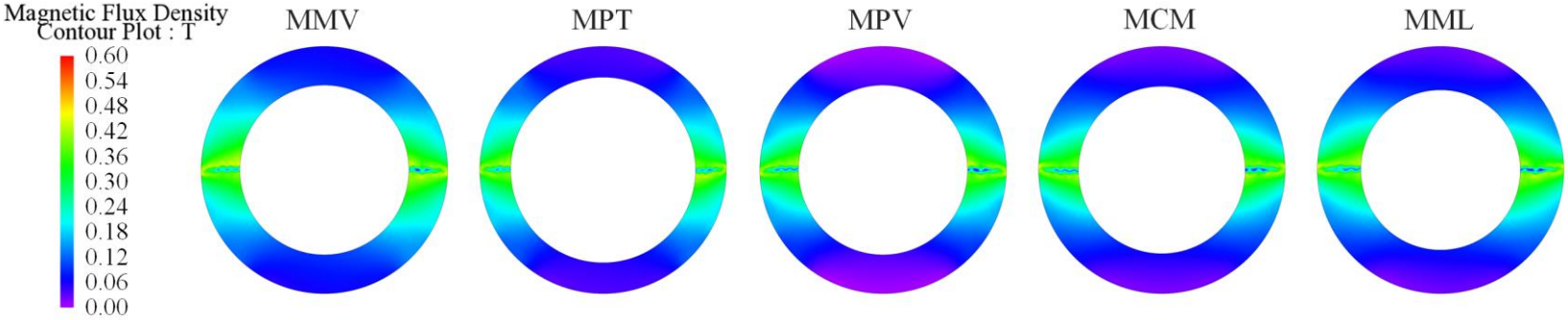

Fig. 24 Magnetic flux density distribution at the maximum speed for the five HS-PMSMs.

Regarding machine losses, AC copper losses, iron losses and sleeve eddy current losses have been evaluated at rated speed, as reported in Fig. 25. In particular, sleeve eddy current losses have been included because they are not negligible compared to the other contributions [45], [46]. This is not in contrast with the initial assumption of considering the sleeve as an additional airgap from a magnetic point of view because the CFRP has almost the same magnetic permeability of the air. Hence, Fig. 25 reveals that the main contribution comes from copper losses due to the significant skin and proximity effects. The latter makes the current density higher, by increasing the effective phase resistance up to 17 times. Moreover, it has to be noticed that copper losses are under estimated, since end-windings are not considered. The minimum copper losses are achieved by MPT because the minimum current value corresponding to MCM is more than counterbalanced by the higher average phase resistance.

In conclusion, overall FEA results are reported in TABLE XII, in which the average resistance values are derived by equating the copper losses results achieved by FEA with the analytical expression achieved by the 3PO control strategy reported in [28].

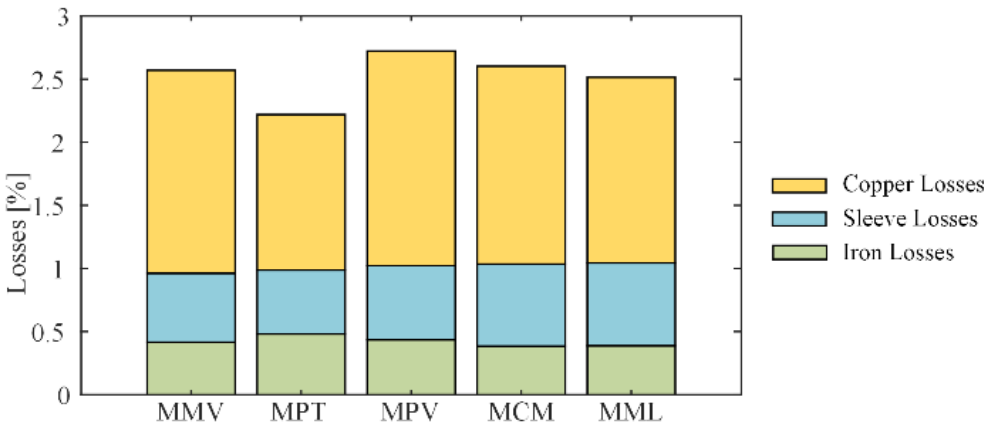

Fig. 25 Overall losses histogram (in %) achieved at rated speed for the five HS-PMSM configurations.

TABLE XII RESULTS OF FINITE ELEMENT ANALYSES

Description	**Symbol**	**Unit**	**MMV**	**MPT**	**MPV**	**MCM**	**MML**
Maximum speed	$\omega_{m,max}$	krpm	100	100	100	97.5	100
Contact pressure @ $\omega_{m,max}$	$p_o^{(L1)}$	MPa	42	23	42	67	38
Tensile strenght @ $\omega_{m,max}$	$\sigma_{eq}^{(L3)}$	MPa	1760	1758	1758	1432	1445
Average torque @$\omega_{m,n}$	$T_{e,n}$	Nm	12.65	12.75	12.71	12.39	12.48
Average torque @$\omega_{m,max}$	$T_{e,max}$	Nm	0.968	0.589	0.866	0.875	0.982
Cogging torque @ $\omega_{m,n}$	δT_e	Nm	0.23	0.24	0.17	0.10	0.09
Average phase resistance @$\omega_{m,n}$	R_n	Ω	0.021	0.015	0.029	0.031	0.025
Average phase resistance @$\omega_{m,max}$	R_{max}	Ω	0.174	0.138	0.248	0.213	0.162
Phase inductance	L	mH	0.544	0.546	0.694	0.748	0.630
Torque current (3PO, $\omega_{m,max}$)	i_t	pu	0.08	0.10	0.05	0.01	0.06
Flux current (3PO, $\omega_{m,max}$)	i_f	pu	-1.20	-1.34	-1.18	-1.10	-1.08
Iron losses @$\omega_{m,n}$	$P_{fe,n}$	kW	0.167	0.193	0.174	0.154	0.155
Iron losses @$\omega_{m,max}$	$P_{fe,max}$	kW	0.391	0.494	0.392	0.246	0.315
Sleeve Joule losses @$\omega_{m,n}$	$P_{b,n}$	kW	0.218	0.202	0.235	0.260	0.263
Sleeve Joule losses @$\omega_{m,max}$	$P_{b,max}$	kW	1.501	1.563	1.516	1.379	1.474
Winding Joule losses @$\omega_{m,n}$	$P_{b,n}$	kW	0.643	0.493	0.680	0.627	0.588
Winding Joule losses @$\omega_{m,max}$	P_j	kW	5.300	4.687	5.850	4.317	3.844

III. HIGH-SPEED PMSM – CONTROL

The HS-PMSM considered in this thesis is designed with trapezoidal back-emfs; the permanent magnet synchronous machines characterized by this specific back-emf shape are generally called Permanent Magnet Brushless DC Machine (PMBDCM) and controlled through Current Commutation Control approaches (CCC). However, despite their simplicity, these conventional control schemes are unable to provide adequate performances, especially in terms of average torque, torque ripple and wide constant power speed operation. Consequently, in order to exploit the designed HS-PMSM properly, an alternative "three-phase-on" control strategy (3PO) has been selected [27], [28]. In particular, 3PO allows the HS-PMSM to operate with better efficiency, lower losses and reduced torque ripple compared to conventional CCC. For this reason, this control strategy has been analyzed accurately, by proposing some improvements in order to further increase its performances, as detailed in the following.

III.1. PMBDCM modelling

Referring to the schematic representation of a three-phase PMBDCM depicted in Fig. 26, the corresponding phase voltage equations of the continuous-time mathematical model can be expressed in terms of phase quantities as

$$v_{ph} = r\, i_{ph} + L\frac{di_{ph}}{dt} + M\frac{dI_0}{dt} + e_{ph} \tag{III.1.1}$$

where v_{ph} and i_{ph} denote phase voltage and current vectors, e_{ph} is the back-emf vector due to permanent magnets, and I_0 is the zero-sequence current vector:

$$v_{ph} = \begin{bmatrix} v_u \\ v_v \\ v_w \end{bmatrix}, \quad i_{ph} = \begin{bmatrix} i_u \\ i_v \\ i_w \end{bmatrix}, \quad e_{ph} = \begin{bmatrix} e_u \\ e_v \\ e_w \end{bmatrix}, \quad I_0 = \begin{bmatrix} i_0 \\ i_0 \\ i_0 \end{bmatrix}, \quad i_0 = i_u + i_v + i_w\,. \tag{III.1.2}$$

Still referring to (III.1.1), r and L are the phase resistance and the synchronous inductance respectively, while M is the mutual inductance. Denoting by ϑ the electrical rotor position, the e_{ph} components are ideally characterized by trapezoidal shapes, as depicted in Fig. 27. Thus, in order to determine an analytical expression of e_{ph}, the electrical period can be split into six sectors at first, as highlighted in TABLE XIII. In each sector, the phase terminals $\{u,v,w\}$ can be denoted by the indexes $\{x,y,z\}$ alternatively, while σ is a suitable sign variable. Subsequently, an appropriate position variable can be introduced as

$$\vartheta_{pu} = \left(\frac{3}{\pi}\vartheta - \frac{1}{2}\right) \% \, 1 \tag{III.1.3}$$

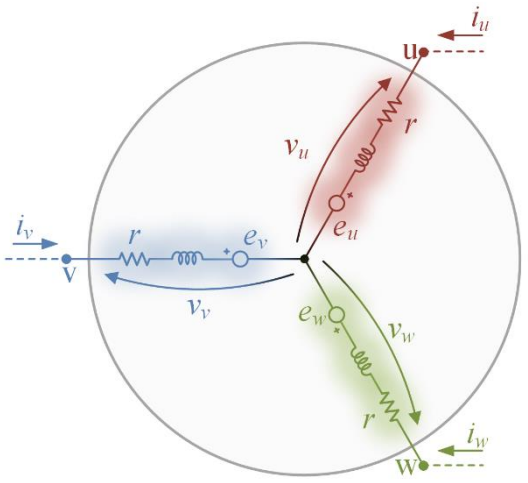

Fig. 26 Schematic representation of a three-phase PMBDCM.

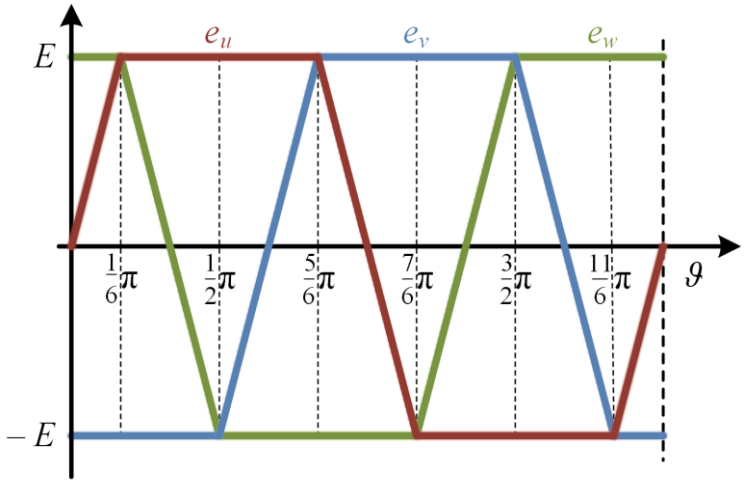

Fig. 27 Ideal back-emf shapes of a three-phase PMBDCM.

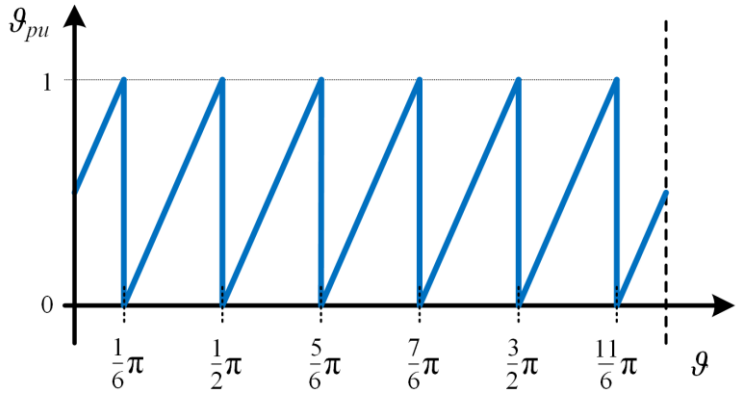

Fig. 28 The evolution of ϑ_{pu} with ϑ within an electrical period.

TABLE XIII PMBDCM OPERATING SECTORS

Sector	Electrical Rotor Position Range	Three-phase Terminals			σ
		u	***v***	***w***	
I	$\frac{1}{6}\pi \le \vartheta < \frac{1}{2}\pi$	x	y	z	+1
II	$\frac{1}{2}\pi \le \vartheta < \frac{5}{6}\pi$	y	z	x	–1
III	$\frac{5}{6}\pi \le \vartheta < \frac{7}{6}\pi$	z	x	y	+1
IV	$\frac{7}{6}\pi \le \vartheta < \frac{3}{2}\pi$	x	y	z	–1
V	$\frac{3}{2}\pi \le \vartheta < \frac{11}{6}\pi$	y	z	x	+1
VI	$\frac{11}{6}\pi \le \vartheta, \vartheta < \frac{1}{6}\pi$	z	x	y	–1

where the operator % provides the fractional part of the division only. As a result, ϑ_{pu} always varies within [0,1) over the overall electrical period and it resets whenever a change of sector occurs, as highlighted in Fig. 28. As a result, (III.1.1) can be better expressed in terms of *{x,y,z}* rather than *{u,v,w}*, leading to

$$v = r\,i + L\frac{di}{dt} - M\frac{dI_0}{dt} + e \tag{III.1.4}$$

where *v*, *i*, *e* and I_0 can be expressed as

$$v = \begin{bmatrix} v_x \\ v_y \\ v_z \end{bmatrix} \quad , \quad i = \begin{bmatrix} i_x \\ i_y \\ i_z \end{bmatrix} \quad , \quad e = \sigma E \begin{bmatrix} 1 \\ -1 \\ 1-2\vartheta_{pu} \end{bmatrix} \quad , \quad I_0 = \begin{bmatrix} i_0 \\ i_0 \\ i_0 \end{bmatrix} \quad , \quad i_0 = i_x + i_y + i_z \ . \tag{III.1.5}$$

In particular, *E* is the back-emf magnitude, expressed as

$$E = p\,\omega_m\,\Lambda \tag{III.1.6}$$

where ω_m is the rotor speed, *p* denotes the number of pole pairs and Λ is the flux linkage due to permanent magnets only. Hence, based on (III.1.4) through (III.1.6), the PMBDCM torque can be expressed as

$$T_e = \sigma p \Lambda \left(i_x - i_y + \left(1 - 2\vartheta_{pu}\right) i_z \right). \tag{III.1.7}$$

Whereas the Joule losses are

$$P_J = r\left(i_x^2 + i_y^2 + i_z^2\right) \ . \tag{III.1.8}$$

III.2. PMBDCM control approaches

III.2.1. Current Commutation Control (CCC)

The most popular and traditionally used control approach for three-phase PMBDCMs consists of supplying only two phases at once over each sector, i.e. a constant current should flow through the *x* and *y* phases, while the *z* phase should be idle. Consequently, no zero-sequence current should flow and, thus, the reference current vector to be employed for any Current Commutation Control approach (CCC) can be defined as

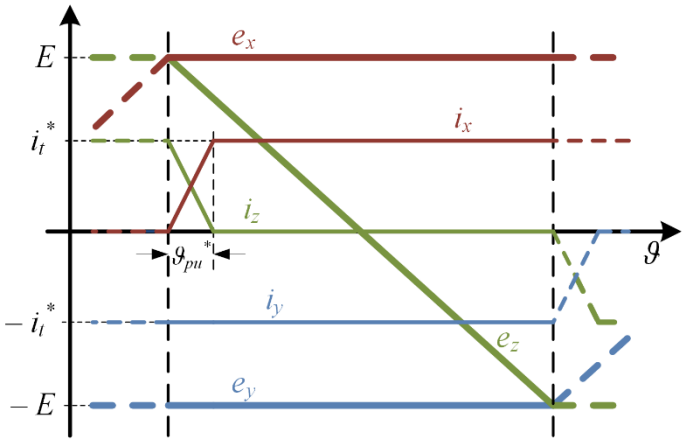

Fig. 29 An example of a PMBDCM current commutation.

$$i^*\big|_{CCC} = \sigma i_t^* \cdot \begin{bmatrix} 1 \\ -1 \\ 0 \end{bmatrix} \tag{III.2.1}$$

in which i_t^* denotes the reference torque current. Therefore, the substitution of (III.2.1) in (III.1.7) and (III.1.8) yields

$$\begin{aligned} T_e^*\big|_{CCC} &= 2p\Lambda \cdot i_t^* \\ P_J^*\big|_{CCC} &= 2r \cdot \left(i_t^*\right)^2 . \end{aligned} \tag{III.2.2}$$

Based on (III.2.2), it could be stated that CCC does not provide any torque ripple theoretically. However, as soon as a change of sector occurs, appropriate current commutations have to be accomplished in accordance with both TABLE XIII and (III.2.1) . In particular, i_x and i_z have to be driven to their corresponding reference values, possibly holding i_y constant, as shown in Fig. 29. It is worth noting that current commutation cannot be performed instantaneously, thus it spreads for a certain share of the sector (ϑ_{pu}^*), which increases with the rotor speed. Over current commutations, the following relationship should be thus satisfied:

$$\begin{aligned} &\frac{di_y}{dt} = 0 \quad , \quad \frac{di_x}{dt} = -\frac{di_z}{dt} \\ &i_y = -\sigma i_t^* \quad , \quad i_x = \sigma i_t^* - i_z \quad . \end{aligned} \tag{III.2.3}$$

Therefore, by substituting (III.2.3) in both (III.1.7) and (III.1.8), the following relationships are achieved:

$$\begin{aligned} T_e\big|_{CCC} &= T_e^*\big|_{CCC} - 2p\Lambda\cdot\vartheta_{pu}\cdot\sigma i_z \\ P_J\big|_{CCC} &= P_J^*\big|_{CCC} - 2r\cdot\sigma i_z\cdot\left(i_t^* - \sigma i_z\right) . \end{aligned} \tag{III.2.4}$$

Since σi_z is always positive over each sector, (III.2.4) states that both T_e and P_J decrease over each current commutation compared to their corresponding reference values. As a result, although (III.2.2) states that both T_e and P_J should be constant within each sector, (III.2.4) reveals that their corresponding average values are affected by current commutations because they both depend on the z current. In order to explicit the dependency of (III.2.4) from ϑ_{pu}^*, the following relationship can be introduced:

$$i_z = \sigma\, i_t^*\left(1-\frac{\vartheta_{pu}}{\vartheta_{pu}^*}\right), \quad \vartheta_{pu}\in\left[0,\vartheta_{pu}^*\right]. \tag{III.2.5}$$

Therefore, the substitution of (III.2.5) in (III.2.4) yields

$$\begin{aligned} T_e\big|_{CCC} &= T_e^*\big|_{CCC}\left(1-\vartheta_{pu}\left(1-\frac{\vartheta_{pu}}{\vartheta_{pu}^*}\right)\right), \quad \vartheta_{pu}\in\left[0,\vartheta_{pu}^*\right] \\ P_J\big|_{CCC} &= P_J^*\big|_{CCC}\left(1-\frac{\vartheta_{pu}}{\vartheta_{pu}^*}\left(1-\frac{\vartheta_{pu}}{\vartheta_{pu}^*}\right)\right), \quad \vartheta_{pu}\in\left[0,\vartheta_{pu}^*\right] . \end{aligned} \tag{III.2.6}$$

Hence, different considerations have to be made for T_e and P_J. In fact, the latter experiences a minimum per-unit value of 0.75 whatever ϑ_{pu}^* is; while the minimum value of T_e is strictly related to ϑ_{pu}^*, as highlighted by the following expressions:

$$\begin{aligned} \underset{0\le\vartheta_{pu}\le\vartheta_{pu}^*}{min}\left\{T_e\big|_{CCC}\right\} &= \left(1-\frac{1}{4}\vartheta_{pu}^*\right)T_e^*\big|_{CCC} \\ \underset{0\le\vartheta_{pu}\le\vartheta_{pu}^*}{min}\left\{P_J\big|_{CCC}\right\} &= \frac{3}{4}\cdot P_J^*\big|_{CCC} . \end{aligned} \tag{III.2.7}$$

At low-speed operation, ϑ_{pu}^* is quite small, thus T_e is almost constant over current commutations and, thus, torque ripple is quite negligible. At high-speed operation, ϑ_{pu}^* increases significantly with the rotor speed, leading to significant torque ripple. Considering average values of both T_e and P_J, this are affected by ϑ_{pu}^*, namely, they decrease as ϑ_{pu}^* increases, as highlighted by the following expressions:

$$\begin{aligned}\bar{T}_e\big|_{CCC} &= \int_0^1 T_e\big|_{CCC}\, d\vartheta_{pu} = T_e^*\big|_{CCC}\left(1-\frac{1}{6}\left(\vartheta_{pu}^*\right)^2\right)\\ \bar{P}_J\big|_{CCC} &= \int_0^1 P_J\big|_{CCC}\, d\vartheta_{pu} = P_J^*\big|_{CCC}\left(1-\frac{1}{6}\vartheta_{pu}^*\right).\end{aligned} \tag{III.2.8}$$

Consequently, torque ripple occurring by CCC may be quite relevant at rated speed, thus leading to reduced PMBDCM torque capability [28]. This represents one of the most important drawback of CCC, which prevents PMBDCM to be widely employed in high-performance applications. This issue has led to the development of alternative control solutions for improving PMBDCM performances within wide speed ranges, among which the "three-phase-on" control approach (3PO) presented in the next subsection.

III.2.2. Three-phase-on control approach (3PO)

The three-phase-on control approach proposed in [27] suggested synthesizing the reference current vector by imposing constant torque and minimum Joule losses constraints at the same time:

$$\begin{aligned}T_e &= T_e^* = 2p\Lambda\cdot i_t^*\\ P_J^* &= \min_{T_e=T_e^*}\{P_J\}\ .\end{aligned} \tag{III.2.9}$$

Based on (III.1.7) and assuming a floating neutral point of the isolated star-connected PMBDCM winding at first ($i_0 = 0$), the following current constraints can be achieved:

$$\begin{aligned}i_x - i_y + \left(1-2\vartheta_{pu}\right)i_z &= 2\cdot\sigma i_t^*\\ i_x + i_y + i_z &= 0\ .\end{aligned} \tag{III.2.10}$$

Therefore, based on (III.2.10), both i_x and i_y can be expressed as a function of i_z, leading to

$$\begin{aligned}i_x &= -\left(1-\vartheta_{pu}\right)i_z + \sigma i_t^*\\ i_y &= -\vartheta_{pu}\, i_z - \sigma i\ .\end{aligned} \tag{III.2.11}$$

Hence, by substituting (III.2.11) in (III.1.8), P_J can be expressed as a function of i_z only:

$$P_J = 2r\left(\left(1-\vartheta_{pu}+\vartheta_{pu}^2\right)i_z^2 - \sigma i_t^*\left(1-2\vartheta_{pu}\right)i_z + \left(i_t^*\right)^2\right)\ . \tag{III.2.12}$$

As a result, by minimizing (III.2.12) with respect to i_z, the following reference profile is achieved:

$$i_z^* = \sigma i_t^* \frac{1-2\vartheta_{pu}}{2\left(1-\vartheta_{pu}+\vartheta_{pu}^2\right)} \ . \tag{III.2.13}$$

Hence, the substitution of (III.2.13) in (III.2.11) enables the achievement of the following optimal reference current vector as

$$i^*\big|_{3PO} = \sigma i_t^* \frac{1}{2\left(1-\vartheta_{pu}+\vartheta_{pu}^2\right)} \begin{bmatrix} 1+\vartheta_{pu} \\ -\left(2-\vartheta_{pu}\right) \\ 1-2\vartheta_{pu} \end{bmatrix}. \tag{III.2.14}$$

The evolutions of i^* within a generic odd sector is depicted in Fig. 30. This highlights that i_x equals i_z at the start of each sector; since the same applies also for even sectors, current commutations do not occur further. In addition, by substituting (III.2.14) in (III.1.7) and (III.1.8), reference torque and Joule losses can be achieved respectively as

$$\begin{aligned} T_e\big|_{3PO} &= 2p\Lambda \cdot i_t^* \\ P_J\big|_{3PO} &= \frac{3}{2} r \cdot \frac{\left(i_t^*\right)^2}{1-\vartheta_{pu}+\vartheta_{pu}^2} \end{aligned} \tag{III.2.15}$$

their average values being

$$\begin{aligned} \bar{T}_e\big|_{3PO} &= \int_0^1 T_e\big|_{3PO}\, d\vartheta_{pu} = 2p\Lambda \cdot i_t^* \\ \bar{P}_J\big|_{3PO} &= \int_0^1 P_J\big|_{3PO}\, d\vartheta_{pu} = \frac{\pi}{\sqrt{3}} r \cdot \left(i_t^*\right)^2 \ . \end{aligned} \tag{III.2.16}$$

In order to compare 3PO to CCC, (III.2.2) can be combined suitably with (III.2.16), leading to

$$\begin{aligned} \bar{T}_e\big|_{3PO} &= T_e^*\big|_{CCC} \\ \bar{P}_J\big|_{3PO} &= \frac{\pi}{2\sqrt{3}} \cdot P_J^*\big|_{CCC} \ . \end{aligned} \tag{III.2.17}$$

Hence, the comparison between (III.2.17) and (III.2.8) reveals that 3PO is able to guarantee the same constant torque value over the overall electrical period, it being also able to reduce average Joule losses by about 9% compared to CCC [27], [28]. In conclusion, it is worth noting that 3PO should be employed along with appropriate sensorless algorithms [29] in order to avoid the need of high-resolution position sensors, which are expensive and would lead to excessive cost increase compared to CCC solutions.

III.2.3. Improved 3PO

The optimal reference currents expressed by (III.2.14) are achieved on condition of star-connected winding with a floating neutral point; consequently, no zero-sequence currents can be injected. This does not generally affect torque capability of Permanent Magnet Brushless AC Machines (PMBACM) because their back-emfs do not generally present any zero-sequence component. However, this is not the case of PMBDCM, for which the sum of the back-emfs equals zero in the middle of each sector only, as easy detectable by (III.1.5). Therefore, in order to increase PMBDCM exploitation further, an improved 3PO is proposed (3PO-N): it is still based on (III.2.9) but it exploits the connection of the neutral point in order to allow suitable zero-sequence current injection. As a result, given (III.2.9), (III.2.10) becomes

$$\begin{aligned} & i_x - i_y + \left(1 - 2\vartheta_{pu}\right) i_z = 2 \cdot \sigma i_t^* \\ & i_x + i_y + i_z = i_0 \ . \end{aligned} \tag{III.2.18}$$

Therefore, i_x and i_y can be expressed as a function of i_z and i_0 as

$$\begin{aligned} i_x &= -\left(1 - \vartheta_{pu}\right) i_z + \sigma i_t^* + \frac{1}{2} i_0 \\ i_y &= -\vartheta_{pu}\, i_z - \sigma i_t^* + \frac{1}{2} i_0 \ . \end{aligned} \tag{III.2.19}$$

Hence, by substituting (III.2.19) in (III.1.8), P_J can be expressed as a function of i_z and i_0:

$$P_J = 2r\left(\left(1 - \vartheta_{pu} + \vartheta_{pu}^2\right) i_z^2 - \left(\sigma i_t^* \left(1 - 2\vartheta_{pu}\right) + \frac{1}{2} i_0\right) i_z + \left(\left(i_t^*\right)^2 + \frac{1}{4} i_0^2\right)\right) . \tag{III.2.20}$$

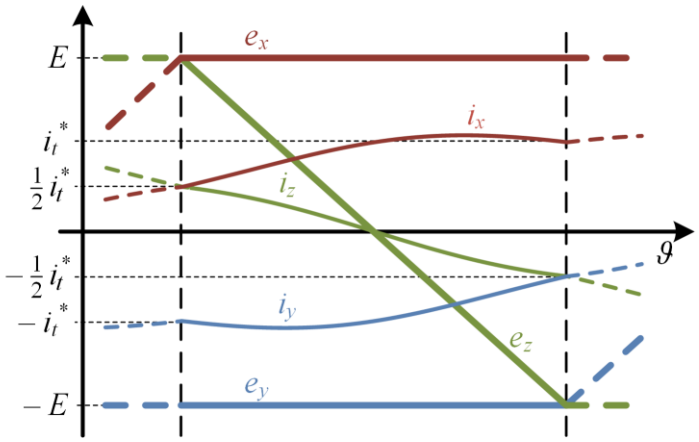

Fig. 30 The 3PO reference current profiles within odd sectors.

By minimizing (III.2.20) with respect to both i_z and i_0, the following expressions are achieved:

$$\begin{aligned} i_z &= \frac{\sigma i_t^* \left(1-2\vartheta_{pu}\right)}{2\left(1-\vartheta_{pu}+\vartheta_{pu}^2\right)} + \frac{i_0}{4\left(1-\vartheta_{pu}+\vartheta_{pu}^2\right)} \cdot \\ i_0 &= i_z \ . \end{aligned} \tag{III.2.21}$$

Therefore, the combination of (III.2.21) to each other yields:

$$i_z^* = i_0^* = \sigma i_t^* \frac{2\left(1-2\vartheta_{pu}\right)}{3-4\vartheta_{pu}+4\vartheta_{pu}^2} . \tag{III.2.22}$$

As a result, the substitution of (III.2.22) in (III.2.19) enables the achievement of another optimal reference current vector as

$$i^*\big|_{3PO\text{-}N} = \sigma i_t^* \cdot \frac{2}{3-4\vartheta_{pu}+4\vartheta_{pu}^2} \begin{bmatrix} 1 \\ -1 \\ 1-2\vartheta_{pu} \end{bmatrix}, \quad i_0^*\big|_{3PO\text{-}N} = i_z^*\big|_{3PO\text{-}N} . \tag{III.2.23}$$

The new optimal current profiles within a generic odd sector are depicted in Fig. 31. As for 3PO, i_x and i_z share the same value at the start of each odd the sector; since this applies also for even sectors, current commutations are not needed also in this case. In addition, referring to (III.2.23), it can be seen that i_0 equals i_z, as well as i_x equals $-i_y$. Consequently, two different current paths can be identified clearly, as shown in Fig. 32. By substituting (III.2.23) in both (III.1.7) and (III.1.8), T_e and P_J can be expressed as

$$\begin{aligned} T_e\big|_{3PO\text{-}N} &= 2p\Lambda \cdot i_t^* \\ P_J\big|_{3PO\text{-}N} &= 4r \cdot \frac{\left(i_t^*\right)^2}{3-4\vartheta_{pu}+4\vartheta_{pu}^2} . \end{aligned} \tag{III.2.24}$$

While their average values can be determined as

$$\begin{aligned} \bar{T}_e\big|_{3PO\text{-}N} &= \int_0^1 T_e\big|_{3PO-N} \, d\vartheta_{pu} = 2p\Lambda \cdot i_t^* \\ \bar{P}_J\big|_{3PO\text{-}N} &= \int_0^1 P_J\big|_{3PO-N} \, d\vartheta_{pu} = \sqrt{2}\, arctg\left(\frac{\sqrt{2}}{2}\right) \cdot 2r\left(i_t^*\right)^2 . \end{aligned} \tag{III.2.25}$$

Therefore, in order to compare (III.2.25) to (III.2.8), but especially to (III.2.17), (III.2.2)

can be substituted suitably in (III.2.25), leading to

$$\begin{aligned} \bar{T}_e\big|_{3PO\text{-}N} &= T_e^*\big|_{CCC} \\ \bar{P}_J\big|_{3PO\text{-}N} &= \sqrt{2}\, arctg\left(\frac{\sqrt{2}}{2}\right)\cdot P_J^*\big|_{CCC} . \end{aligned} \qquad \text{(III.2.26)}$$

Hence, the comparison between (III.2.17) and (III.2.26) reveals a further PMBDCM exploitation achieved by 3PO-N through the injection of a suitable zero-sequence current component. In particular, 3PO-N is able to guarantee the same constant torque as 3PO, but the Joule losses decreases by about 13% compared to CCC, whereas it decreases by about 9% only by 3PO [47].

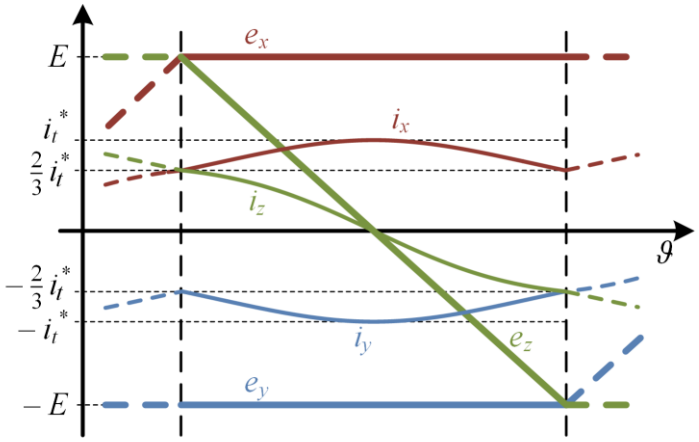

Fig. 31 The optimal reference current profiles by 3PO-N (odd sectors).

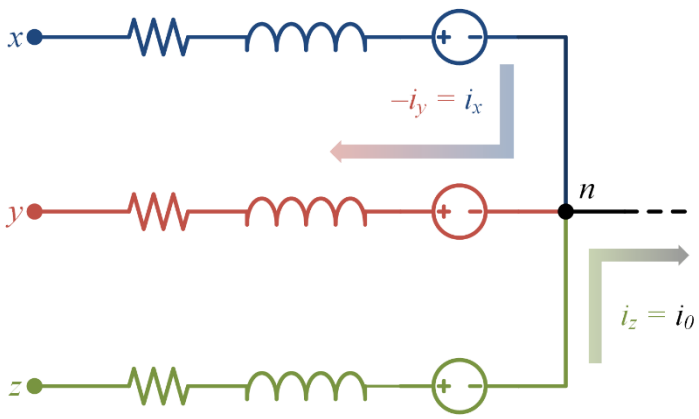

Fig. 32 Schematic representation of the current paths achieved by 3PO-N.

III.2.4. Comparison between PMBDCM and PMBACM performances

In order to highlight the performance improvements achievable by means of the proposed 3PO-N, a comparison analysis between PMBDCM and PMBACM has been performed. In particular, two different scenarios are considered; in the first one (case 1), both PMBACM and PMBDCM have to provide the same torque value, whereas PMBACM and PMBDCM are characterized by the same Joule losses in the second scenario (case 2). In both cases, PMBACM is assumed to be controlled in accordance with Maximum Torque per Ampere control strategy (MTPA) and that no flux weakening operation occurs for both PMBACM and PMBDCM; consequently, PMBACM torque and Joule losses can be expressed respectively as

$$T_e\big|^{PMBACM} = \frac{3}{2} p\Lambda \cdot i_t^* \ , \quad P_J\big|^{PMBACM} = \frac{3}{2} r \cdot \left(i_t^*\right)^2 \tag{III.2.27}$$

their corresponding average values being

$$\bar{T}_e\big|^{PMBACM} = \frac{3}{2} p\Lambda \cdot i_t^* \ , \quad \bar{P}_J\big|^{PMBACM} = \frac{3}{2} r \cdot \left(i_t^*\right)^2 . \tag{III.2.28}$$

TABLE XIV PMBACM VS PMBDCM PERFORMANCES (CASE 1)

	PMBACM	**PMBDCM**		
	MTPA	***CCC***	***3PO***	***3PO-N***
I	1	0.75	0.75	0.75
$\hat{\imath}_{ph}$	1	0.75	0.808	0.75
$\bar{T}_e$	1	1[a]	1	1
$\bar{P}_J$	1	0.75	0.680	0.653

[a] neglecting torque ripple due to current commutations

TABLE XV PMBACM VS PMBDCM PERFORMANCES (CASE 2)

	PMBACM	**PMBDCM**		
	MTPA	***CCC***	***3PO***	***3PO-N***
I	1	0.866	0.909	0.928
$\hat{\imath}_{ph}$	1	0.866	0.979	0.928
$\bar{T}_e$	1	1.155[b]	1.213	1.234
$\bar{P}_J$	1	1	1	1

[b] neglecting torque ripple due to current commutations

Whereas PMBDCM is assumed driven in accordance with CCC, 3PO and 3PO-N alternatively in order to highlight the improvements achievable with the latter. The comparison is performed assuming the same Λ value for both PMBACM and PMBDCM in all scenarios, meaning that both these machines are characterized by the same back-emf magnitude.

The comparison results are summarized in both TABLE XIV and TABLE XV, which refer to case 1 and case 2 respectively. In particular, all the values are reported in per unit with reference to PMBACM quantities for convenience purposes. Focusing on case 1 at first, it can be seen that 3PO-N guarantees the best performances, enabling a Joule losses reduction of about 35% compared to PMBACM. Very similar results are achieved also by means of 3PO, which, however, is characterized by peak phase current ($\hat{\imath}_{ph}$) and average Joule losses slightly greater than 3PO-N. It is worth noting that also CCC shows better performances compared to PMBACM; however, such improvements are counterbalanced by torque ripple due to current commutations, which do not occur over either 3PO or 3PO-N. The effectiveness of 3PO-N is proved also by case 2, in correspondence of which PMBACM and PMBDCM are characterized by the same average Joule losses. In particular, 3PO-N enables a torque increase of about 23% and the peak phase current being reduced by about 7%. Less performance improvements can be achieved by 3PO and CCC, the latter being also affected by torque ripple, as stated before.

III.3. Space Vector Control

In order to implement either 3PO or 3PO-N successfully, a Space Vector Control (SVC) for PMBDCM is needed. Hence, reference is made to a PMBDCM with floating star-connected winding, which is the most popular and common configuration. Consequently, two current vector components have to be identified appropriately. One of these is surely represented by the torque current i_t, whose corresponding optimal profile is defined by (III.2.14) and depicted in Fig. 30. The other current vector component can be determined by imposing the following constraints:

$$\begin{aligned} T_e^* &= 0 \\ P_J^* &= \frac{3}{2} r \cdot \frac{\left(i_f^*\right)^2}{1 - \vartheta_{pu} + \vartheta_{pu}^2} \end{aligned} \tag{III.3.1}$$

where i_f can be defined as the field current. In particular, by comparing (III.2.15) with (III.3.1) and assuming i_f equal to i_t, it can be stated that i_f provides no PMBDCM torque but the same Joule losses of i_t [48]. Consequently, by combining (III.1.7) with (III.3.1),

the following current constraints are achieved:

$$\begin{aligned} & i_x - i_y + \left(1 - 2\vartheta_{pu}\right) i_z = 0 \\ & i_x + i_y + i_z = 0 \ . \end{aligned} \tag{III.3.2}$$

Therefore, it is possible to express both i_x and i_y as a function of i_z as

$$\begin{aligned} & i_x = -\left(1 - \vartheta_{pu}\right) i_z \\ & i_y = -\vartheta_{pu}\, i_z \ . \end{aligned} \tag{III.3.3}$$

Hence, by substituting (III.2.19) in (III.1.8), P_J can be expressed as:

$$P_J = 2r\left(1 - \vartheta_{pu} + \vartheta_{pu}^2\right) i_z^2 \ . \tag{III.3.4}$$

As a result, by imposing (III.3.4) equal to P_J^* expressed by (III.3.1), the i_z reference profile can be easily achieved as

$$i_z^* = \sigma i_f^* \cdot \frac{\sqrt{3}}{2} \cdot \frac{1}{1 - \vartheta_{pu} + \vartheta_{pu}^2} . \tag{III.3.5}$$

The substitution of (III.3.5) in (III.3.3) yields the three-phase reference current profile shown in Fig. 33, which can be expressed as

$$i^* = \sigma i_f^* \cdot \frac{\sqrt{3}}{2} \frac{1}{1 - \vartheta_{pu} + \vartheta_{pu}^2} \begin{bmatrix} -\left(1 - \vartheta_{pu}\right) \\ -\vartheta_{pu} \\ 1 \end{bmatrix} . \tag{III.3.6}$$

Hence, based on both (III.2.14) and (III.3.6), it is possible to express any three-phase current vector as

$$i = \frac{\sigma}{2} \frac{1}{1 - \vartheta_{pu} + \vartheta_{pu}^2} \begin{bmatrix} -\sqrt{3}\left(1 - \vartheta_{pu}\right) & 1 + \vartheta_{pu} \\ -\sqrt{3}\vartheta_{pu} & -\left(2 - \vartheta_{pu}\right) \\ \sqrt{3} & 1 - 2\vartheta_{pu} \end{bmatrix} \begin{bmatrix} i_f \\ i_t \end{bmatrix} \tag{III.3.7}$$

where i_f and i_t represent the field and torque current components. In addition, by substituting (III.3.7) in (III.1.7) and (III.1.8), torque and Joule losses become respectively:

$$\begin{aligned} & T_e = 2p\Lambda \cdot i_t \\ & P_J = \frac{3}{2} r \cdot \frac{i_f^2 + i_t^2}{1 - \vartheta_{pu} + \vartheta_{pu}^2} . \end{aligned} \tag{III.3.8}$$

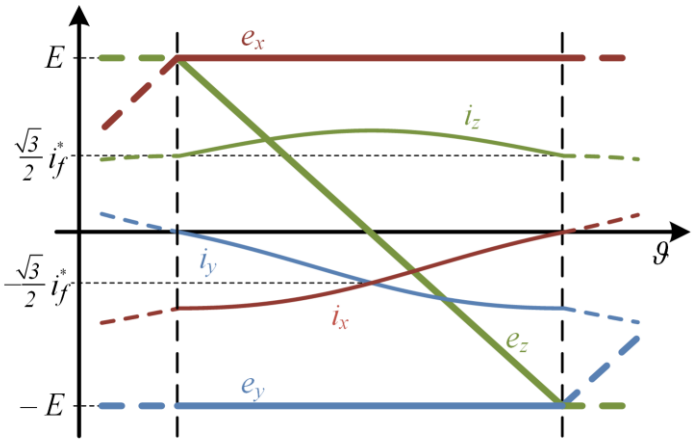

Fig. 33 Three-phase current evolutions in accordance with (III.3.6).

Therefore, both (III.3.7) and (III.3.8) suggest defining a novel *ft* synchronous reference frame in order to enable a simple and effective space vector modeling of PMBDCM, as pointed out in the following subsection.

III.3.1. The ft synchronous reference frame

Based on (III.1.4) and assuming no zero-sequence current component, it is possible to express the PMBDCM voltage equations in terms of space vectors referred to the *αβ* stationary reference frame as

$$v_{\alpha\beta} = r\, i_{\alpha\beta} + L \frac{di_{\alpha\beta}}{dt} + e_{\alpha\beta} \tag{III.3.9}$$

in which:

$$d_{\alpha\beta} = \frac{2}{3}\left(d_x + d_y\, e^{j\frac{2}{3}\pi} + d_z\, e^{j\frac{4}{3}\pi}\right), \quad d \in \{v,i,e\}. \tag{III.3.10}$$

Hence, considering both (III.1.5) and (III.3.7), back-emf and current space vectors can be expressed as

$$e_{\alpha\beta} = j\frac{4}{3} E \left(1 - \vartheta_{pu} + \vartheta_{pu}^2\right) \cdot \gamma \tag{III.3.11}$$

$$i_{\alpha\beta} = \gamma \cdot i_{ft} \tag{III.3.12}$$

where:

$$\gamma = -\frac{\sigma}{2}\frac{1}{1-\vartheta_{pu}+\vartheta_{pu}^2}\left(\sqrt{3}\left(1-\vartheta_{pu}\right)+j\left(1+\vartheta_{pu}\right)\right)$$
$$i_{ft} = i_f + j\cdot i_t\,. \tag{III.3.13}$$

Therefore, based on (III.3.12), it is possible to define a vector transformation from the $\alpha\beta$ to a novel *ft* reference frame and vice versa as

$$\begin{aligned} d_{ft} &= \delta\cdot d_{\alpha\beta} \\ d_{\alpha\beta} &= \gamma\cdot d_{ft} \end{aligned},\quad d\in\{v,i,e\} \tag{III.3.14}$$

where the vector δ is defined as

$$\delta = \frac{\sigma}{2}\left(-\sqrt{3}\left(1-\vartheta_{pu}\right)+j\left(1+\vartheta_{pu}\right)\right),\quad \delta\cdot\gamma = 1\,. \tag{III.3.15}$$

Consequently, by substituting (III.3.14) in (III.3.9), the PMBDCM voltage equations can be usefully expressed in the novel *ft* reference frame as

$$v_{ft} = \left(r+\dot{\vartheta}_{pu}\,L\,\xi_{ft}\right)i_{ft}+L\frac{di_{ft}}{dt}+e_{ft} \tag{III.3.16}$$

in which:

$$\begin{aligned} \xi_{ft} &= \frac{1}{2}\frac{1}{1-\vartheta_{pu}+\vartheta_{pu}^2}\left(\left(1-2\,\vartheta_{pu}\right)+j\sqrt{3}\right) \\ e_{ft} &= j\frac{4}{3}E\left(1-\vartheta_{pu}+\vartheta_{pu}^2\right). \end{aligned} \tag{III.3.17}$$

In conclusion, based on (III.3.16), it is thus possible to design a suitable SVC for PMBDCM in the *ft* reference frame. In particular, an approach similar to that usually followed for PMBACM in the *dq* reference frame can be employed, as detailed in the following subsection.

III.3.2. SVC Design

The block control scheme of the proposed SVC is shown in Fig. 34. In particular, a coordinate transformation of the current vector from the *{u,v,w}* to the novel *ft* synchronous reference frame has to be accomplished based on TABLE XIII, (III.3.10) and (III.3.14). Whereas reference current components can be imposed in accordance with an appropriate Look-Up-Table (LUT), by means of which the most suitable reference

currents are selected in accordance with reference torque and actual speed values, as well as with PMBDCM torque, power, voltage and current constraints. In particular, for each speed value, i_f^* and i_t^* are selected in order to comply with the following constraints:

$$T_e\left(i_t^*\right) \le min\left\{T_e^*, T_{e,n}, \frac{P_n}{\omega_m}\right\} \tag{III.3.18}$$

$$\max_{0\le\vartheta_{pu}<1}\left\{\left|v_{ab}\left(i_f^*, i_t^*\right)\right|\right\} \le V_{dc,n}, \quad ab \in \{xy, yz, zx\} \tag{III.3.19}$$

$$\left|i_{ft}^*\right| \le I_{ft.max} \tag{III.3.20}$$

in which $T_{e,n}$, P_n and $V_{dc,n}$ denote the rated torque, power and DC-link voltage respectively. The latter has been computed at the PMBDCM rated operating condition by using the following relationship:

$$V_{dc,n} = max\left\{\max_{0\le\vartheta_{pu}<1}\left\{\left|v_{xy}\right|\right\}, \max_{0\le\vartheta_{pu}<1}\left\{\left|v_{yz}\right|\right\}, \max_{0\le\vartheta_{pu}<1}\left\{\left|v_{zx}\right|\right\}\right\}\Bigg|_{\substack{i_f=0\\ i_t=I_n\\ \omega_m=\omega_{m,n}}} . \tag{III.3.21}$$

Whereas $I_{ft,max}$ denotes the maximum magnitude of the *ft* current vector, which is related to the maximum average Joule losses. Hence, considering both (III.2.16) and (III.3.8), the following relationship can be achieved:

$$\bar{P}_{J,max} = \frac{\pi}{\sqrt{3}} I_{ft,max}^2 . \tag{III.3.22}$$

In order to guarantee an appropriate tracking of the reference currents, a PI-based control system can be employed, together with appropriate anti-windup filters and feed-forward compensations. The latter can be achieved by introducing the following auxiliary voltage vector:

$$\tilde{v}_{ft} = v_{ft} - \left(\dot{\vartheta}_{pu} L \xi_{ft} \cdot i_{ft} + e_{ft}\right). \tag{III.3.23}$$

Therefore, the combination between (III.3.23) and (III.3.16) yields

$$\tilde{v}_{ft} = r\, i_{ft} + L\frac{di_{ft}}{dt} . \tag{III.3.24}$$

Based on (III.3.24), it is thus possible to size the PI regulators appropriately in order to achieve the desired current dynamic performances.

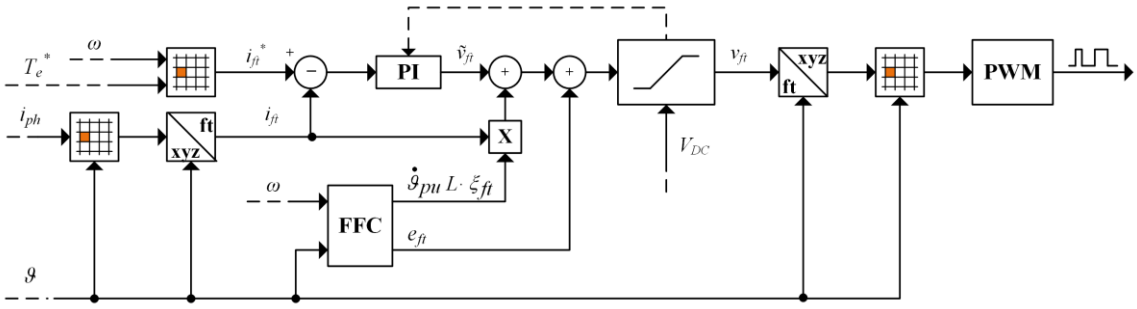

Fig. 34 Block control scheme of the proposed SVC for PMBDCM.

III.4. Simulation Study

III.4.1. Simulation setup

The effectiveness of the proposed SVC has been verified through a simulation study, which has been carried out in the Matlab Simulink environment in accordance with the setup shown in Fig. 35. Regarding the PMBDCM, the HS-PMSM configuration characterized by the minimum PM thickness has been considered (MPT), whose parameters and rated values are reported in TABLE XVI. The PMBDCM is supplied by a three-phase inverter, whose DC-link capacitor is fed by an energy storage system (battery), leading to an overall DC-Link voltage of about 720 V.

The PMBDCM is controlled in accordance with either CCC or SVC for comparison purposes. In particular, CCC consists of regulating the current flowing through the x and y phases by means of the corresponding inverter legs, while the z leg is idle. This goal is achieved by an appropriate PI-based current control loop, which accounts also for feed-forward compensation and anti-windup filter. Whereas the SVC has been implemented in accordance with Fig. 34. In both cases, the bandwidth of the PI regulators has been set to 2 kHz, while the sampling time interval has been chosen equal to 12.8 μs. This leads to an inverter modulation frequency of about 80 kHz.

In conclusion, it is assumed that ϑ and ω are acquired by a high-resolution position sensor in both cases. Although this is not mandatory for CCC, it is much more important for the implementation of the proposed SVC. However, it is worth noting that the employment of a high-resolution position sensor could be avoided by resorting to suitable sensorless algorithms [29]. Consequently, the proposed SVC would not lead to increased costs compared to CCC.

III.4.2. Simulation results

Simulations have regarded PMBDCM low-speed operation at first, namely a step reference torque of 0.2 pu is imposed; hence, a steady state speed value of about 0.2 pu is achieved by setting the damping coefficient and, thus, the load torque properly. The corresponding results (in pu) are depicted from Fig. 36 to Fig. 38. Referring to Fig. 36 at first, it can be seen that current commutations are quickly accomplished by CCC, although an unsuitable spike occurs on the un-commutating current. This drawback does not occur by means of SVC, which is able to guarantee a very good tracking of the reference currents. Consequently, a smoother torque profile is achieved, as highlighted in Fig. 37. This also reveals lower Joule losses achieved by the proposed SVC than by CCC, while the steady state rotor speed value is almost the same in both cases. The improved performances achieved by SVC can be justified by considering the *ft* current component evolutions shown in Fig. 38. In particular, CCC introduces an unsuitable *f* current component, which increases Joule losses without contributing to PMBDCM torque. This is avoided by SVC, which is able to hold i_f constant at zero because no flux weakening operation is required, thus improving PMBDCM exploitation.

Simulations have been then carried out by imposing a reference torque equal to the rated value with the aim of reaching the rated speed at steady state operation. The

TABLE XVI PMBDCM PARAMETERS AND RATED VALUES (HS-PMSM, MPT)

	r	L	p	Λ	$T_{e,n}$	$\omega_{m,n}$
Value	0.011	0.546	1	0.0588	12.7	30
Unit	Ω	mH	-	Vs	Nm	krpm

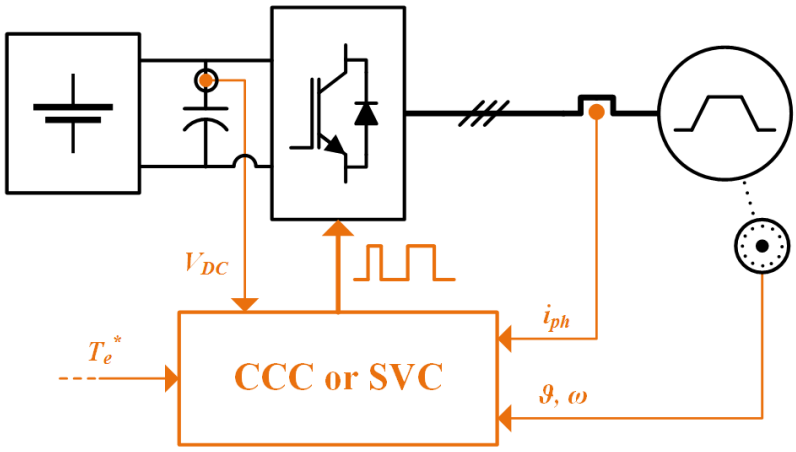

Fig. 35 Simulation setup for testing the proposed SVC in comparison with CCC.

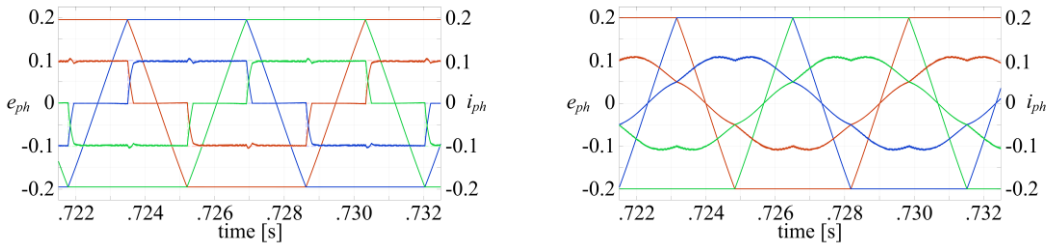

Fig. 36 Phase back-emfs and currents achieved at low speed by CCC (on the left) and SVC (on the right): e_u and i_u (red), e_v and i_v (blue), e_w and i_w (green).

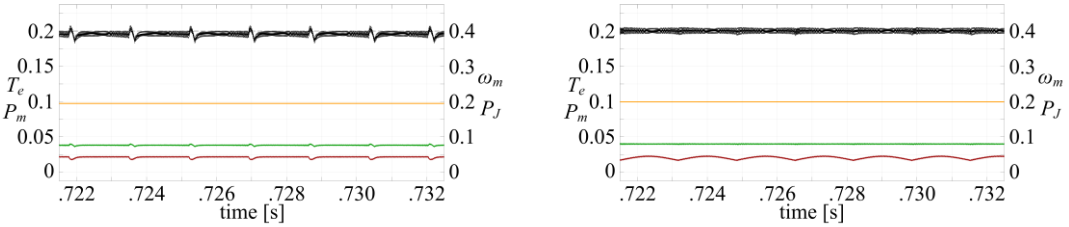

Fig. 37 Torque, speed and powers achieved at low speed by CCC (on the left) and SVC (on the right): T_e (black), ω_m (orange), P_m (green) and P_J (red).

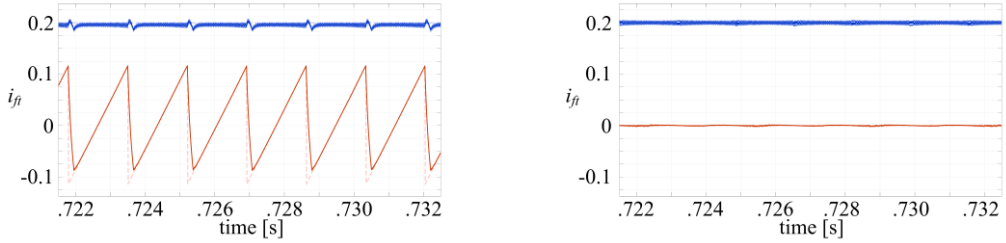

Fig. 38 The *ft* current components achieved at low speed by CCC (on the left) and SVC (on the right): i_f (red) and i_t (blue).

corresponding results (in pu) are depicted in Fig. 39 through Fig. 41. Focusing on CCC performances at first, it can be seen that current commutations spread over a significant part of each sector. Consequently, PMBDCM torque drops down to 0.93 pu and its rated value is almost restored as soon as current commutations are accomplished. Such an unsuitable torque ripple reduces PMBDCM average torque, thus preventing the achievement of the rated speed, as shown in Fig. 40. Much improved performances are achieved by SVC, although torque ripple sometimes occurs also in this case; this is due mainly to the delayed detection of the changes of sector. However, this drawback does not undermine the tracking of the *ft* reference currents excessively, as highlighted in Fig. 41, thus revealing the effectiveness of the proposed control approach.

Finally, the simulations have been carried out by reducing the damping coefficient significantly with the aim of reaching the maximum allowable speed of the PMBDCM.

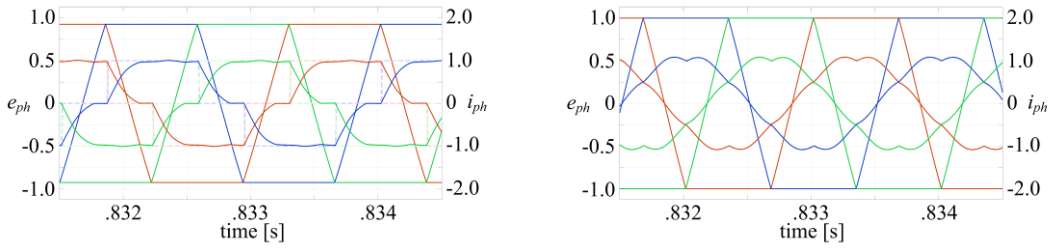

Fig. 39 Phase back-emfs and currents achieved at rated speed by CCC (on the left) and SVC (on the right): e_u and i_u (red), e_v and i_v (blue), e_w and i_w (green).

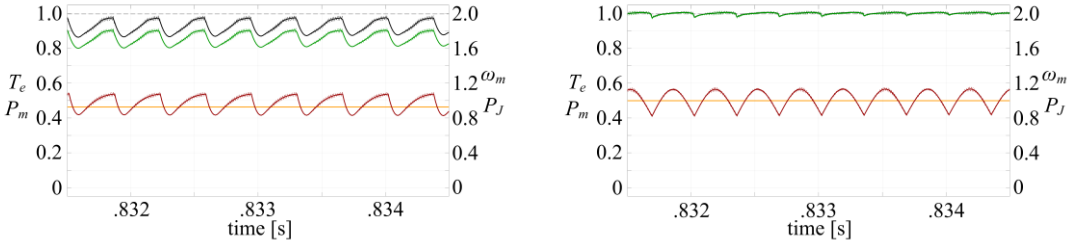

Fig. 40 Torque, speed and powers achieved at rated speed by CCC (on the left) and SVC (on the right): T_e (black), ω_m (orange), P_m (green) and P_J (red).

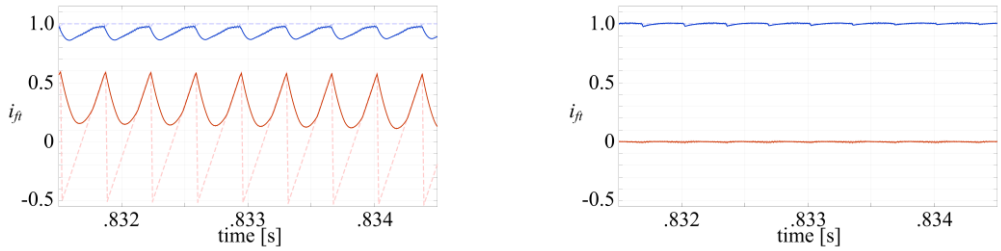

Fig. 41 The *ft* current components achieved at rated speed by CCC (on the left) and SVC (on the right): i_f (red) and i_t (blue).

Focusing on CCC performances at first, these are reported from Fig. 42 to Fig. 48. Considering Fig. 44 and Fig. 45, it can be seen that a short constant power speed range is achieved, which ends at about 1.5 pu. Subsequently, torque and power drop significantly and they are also characterized by high ripple. A maximum speed of about 1.94 pu is finally reached, which is quite far from the design target (about 3.3 times). The weak performances achieved by CCC are due to the evolution of the *f* current component shown in Fig. 45, namely i_f is always positive and characterized by a significant ripple. Considering now steady-state operation (Fig. 46 through Fig. 48), it can be seen that the well-known six-step operation is achieved, which leads to a relatively low maximum speed. This is because no demagnetizing current is injected, namely i_f slightly varies across zero, as highlighted in Fig. 48. Whereas it should be quite negative in order to enable flux-weakening operation properly, as highlighted in Fig. 49. This shows the

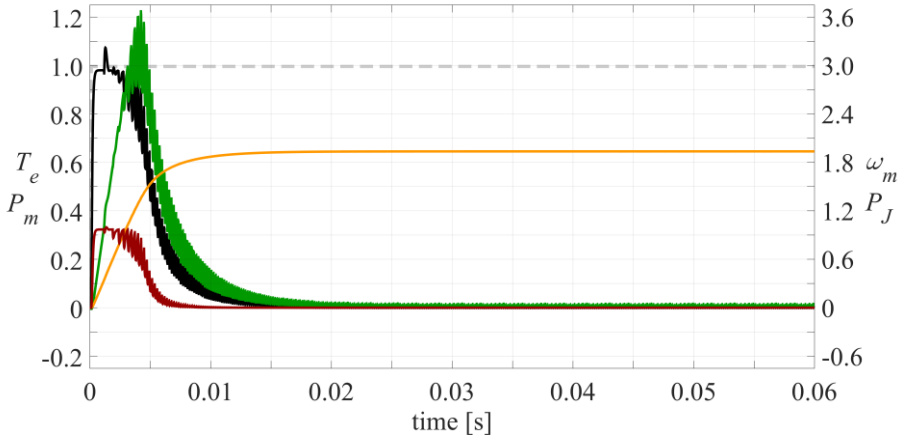

Fig. 42 Torque, speed and powers achieved up to the maximum speed by CCC: T_e (black), ω_m (orange), P_m (green) and P_J (red).

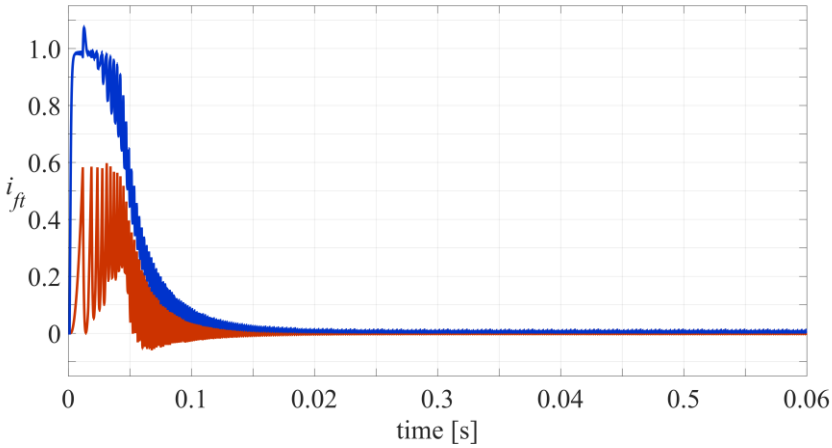

Fig. 43 The *ft* current components achieved up to the maximum speed by CCC: i_f (red) and i_t (blue).

operating boundaries of the PMBDCM in terms of voltage saturation constraint for different speed values in accordance with (III.3.19). Fig. 49 reveals the need of injecting an appropriate i_f negative value for reaching the maximum i_t value and, thus, the maximum torque deliverable by the PMBDCM for a given speed. In particular, i_f should decrease as the speed increase in order to enable a wide PMBDCM constant power region. Consequently, as soon as voltage saturation occurs, PMBDCM performances achieved by CCC decrease significantly, thus preventing the achievement of the target performances, among which the maximum speed.

Much better results are achieved by SVC, as highlighted in Fig. 50 through Fig. 56. In particular, focusing on Fig. 52 and Fig. 53 at first, the reference *ft* current values have been set in accordance with a LUT based on the PMBDCM operating loci shown in Fig. 49. Consequently, as soon as the rotor speed overcomes 1.0 pu, a suitable *f* current

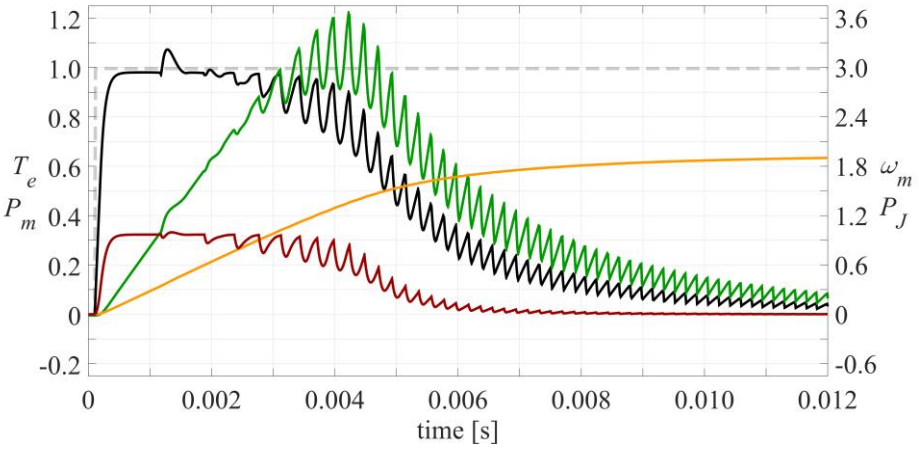

Fig. 44 Magnified view of torque, speed and powers achieved by CCC: T_e (black), ω_m (orange), P_m (green) and P_J (red).

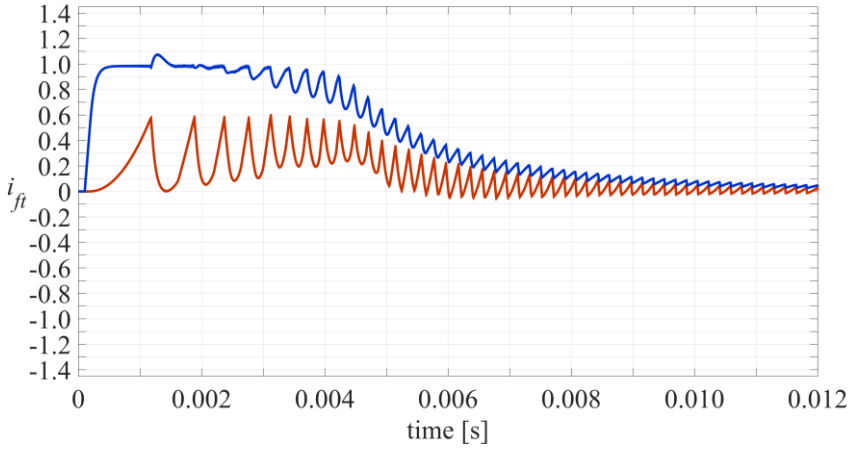

Fig. 45 Magnified view of the *ft* current components achieved by CCC: i_f (red) and i_t (blue).

component is injected in order to enable PMBDCM constant power operation. This operating condition is held until the rotor speed reaches about 1.98 pu, leading to a constant power speed region much wider than by CCC (1.46 pu). As the speed increases beyond 1.9 pu, reduced power operation occurs due to current limitation constraint. However, this does not prevent the achievement of the target maximum speed of about 3.3 pu, as highlighted in Fig. 55. Considering Fig. 56, it can be seen that some ripple occurs on i_f and i_t; both these ripples are due mainly to unpredicted change of sector occurring within the sampling time interval. This issue can be addressed by resorting to more advanced modeling and control technique, as pointed out in [49]. However, it is worth noting that these ripples do not impair the effectiveness of the proposed SVC, which enables much higher PMBDCM performances than conventional CCC, especially at high-speed operation. Consequently, SVC is more suited than CCC as the target control approach for the designed HS-PMSM.

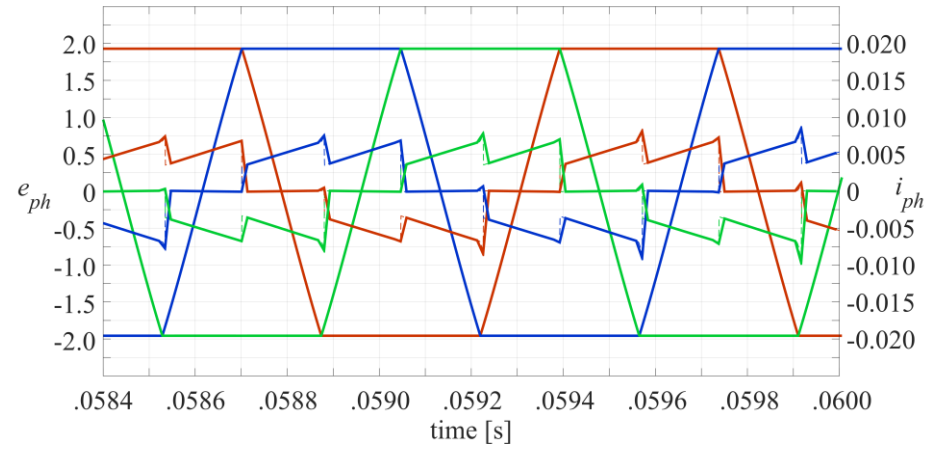

Fig. 46 Phase back-emfs and currents achieved at maximum speed by CCC: e_u and i_u (red), e_v and i_v (blue), e_w and i_w (green).

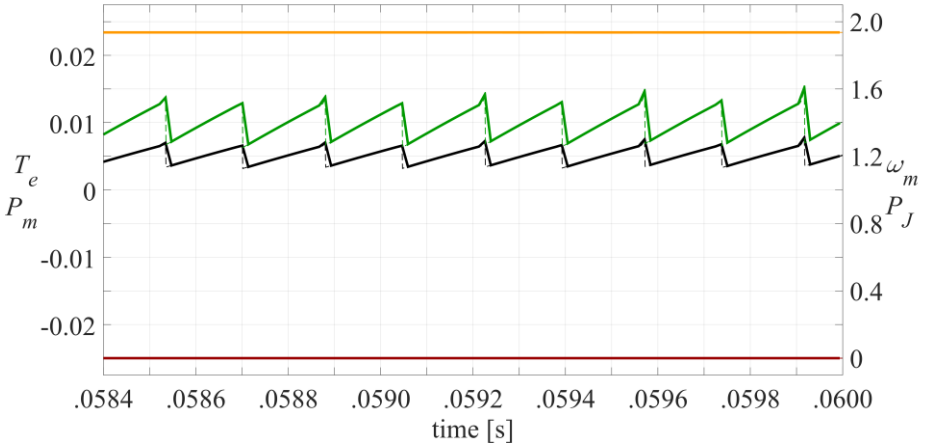

Fig. 47 Torque, speed and powers achieved at maximum speed by CCC: T_e (black), ω_m (orange), P_m (green) and P_J (red).

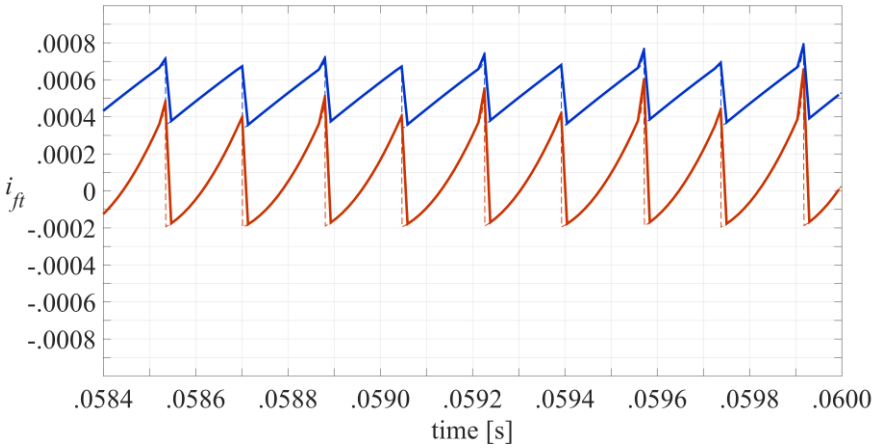

Fig. 48 The *ft* current components achieved at maximum speed by CCC: i_f (red) and i_t (blue).

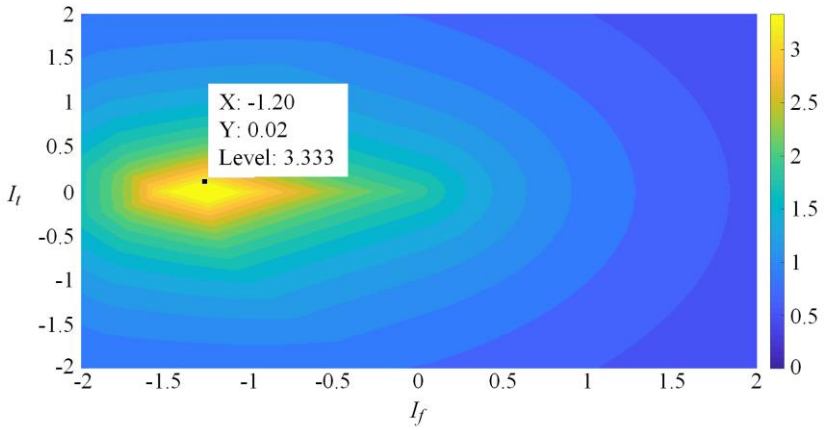

Fig. 49 PMBDCM operating loci (voltage saturation constraint) on the (i_f, i_t) plane at different speed values (colorbar).

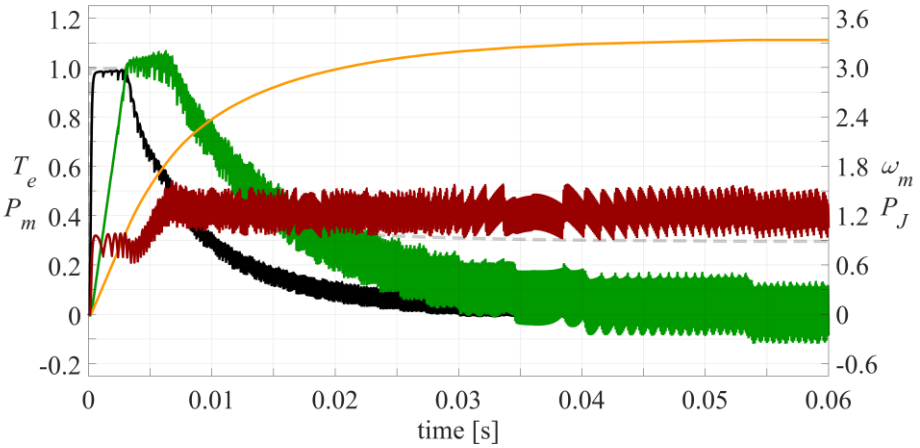

Fig. 50 Torque, speed and powers achieved up to the maximum speed by SVC: T_e (black), ω_m (orange), P_m (green) and P_J (red).

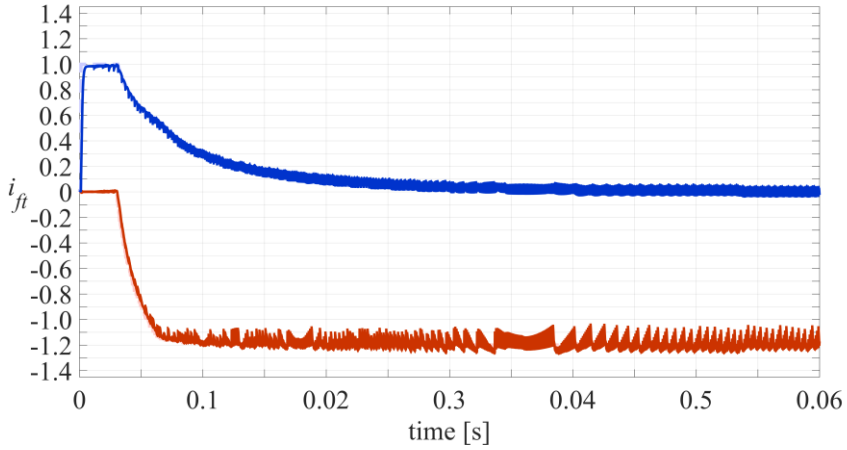

Fig. 51 The *ft* current components achieved up to maximum speed by SVC: i_f (red) and i_t (blue).

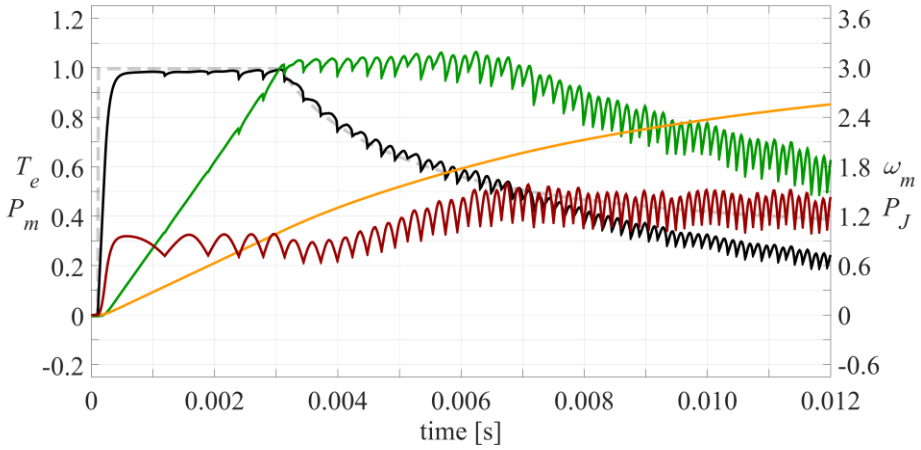

Fig. 52 Magnified view of torque, speed and powers achieved by SVC: T_e (black), ω_m (orange), P_m (green) and P_J (red).

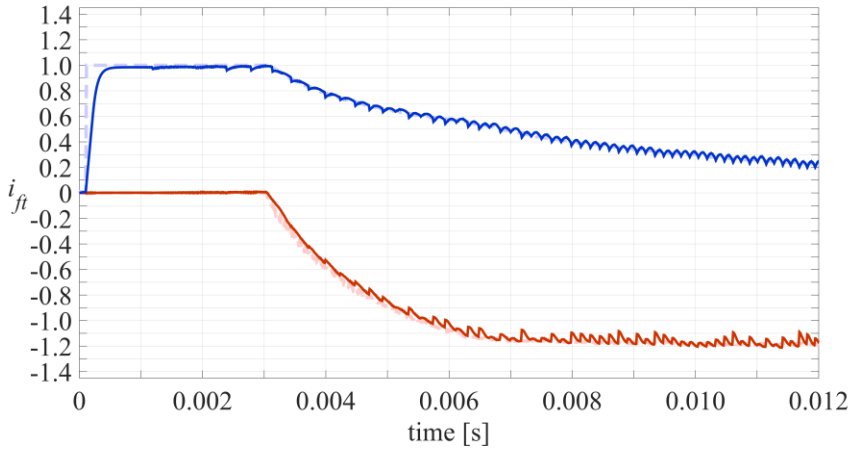

Fig. 53 Magnified view of the *ft* current components achieved by SVC: i_f (red) and i_t (blue).

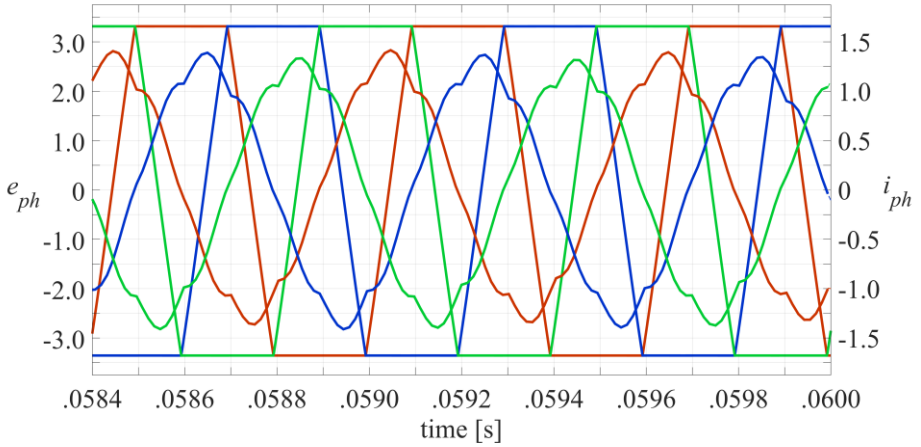

Fig. 54 Phase back-emfs and currents achieved at maximum speed by SVC: e_u and i_u (red), e_v and i_v (blue), e_w and i_w (green).

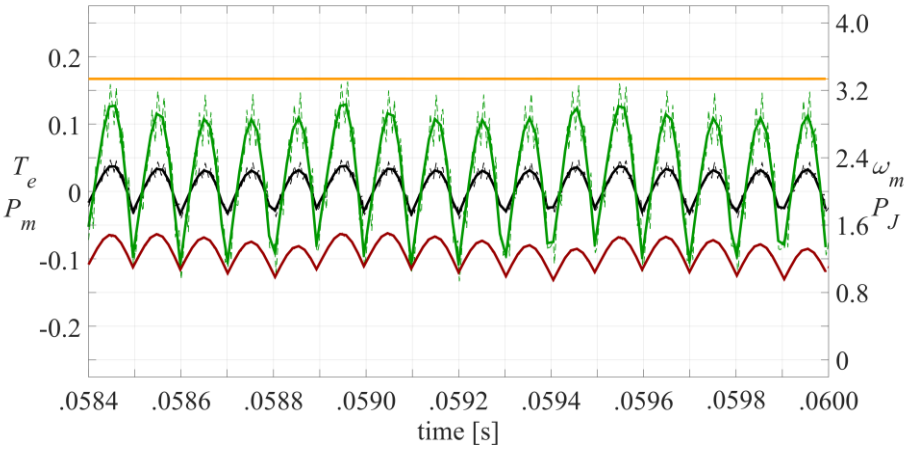

Fig. 55 Torque, speed and powers achieved at maximum speed by SVC: T_e (black), ω_m (orange), P_m (green) and P_J (red).

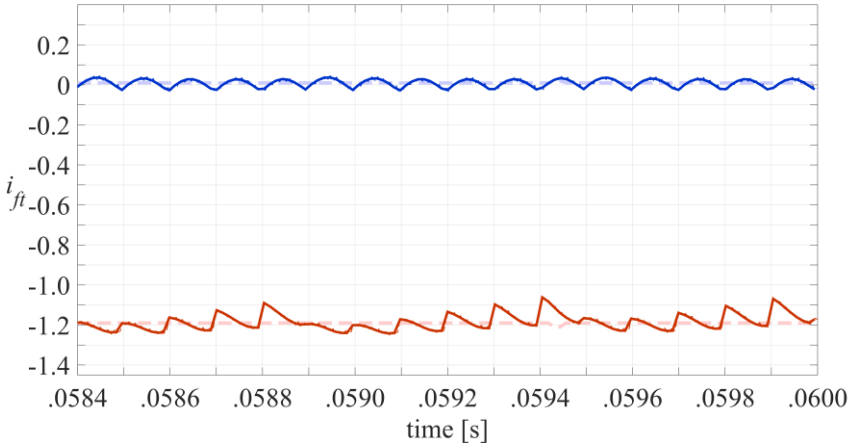

Fig. 56 The *ft* current components achieved at maximum speed by SVC: i_f (red) and i_t (blue).

IV. CONCLUSIONS

This PhD dissertation has regarded design and control of a High-Speed Ferrite-based Permanent Magnet Synchronous Machine (HS-PMSM) for automotive application. In particular, a sleeved surface-mounted PMSM configuration has been chosen with the aim of achieving high rated and maximum speeds (30 and 100 krpm respectively). In addition, ferrite PMs have been considered with the aim of avoiding the use of rare-earth PMs, which are characterized by reduced availability and price fluctuation issues. Finally, trapezoidal-shaped emfs have been selected as the best solution for enabling higher torque density and/or better efficiency on condition that advanced control algorithms are employed.

The first part of this PhD dissertation has focused on both HS-PMSM mechanical and electromagnetic modelling, based on which an analytical multi-parameter design procedure has been developed. This enables a fast and effective HS-PMSM preliminary design by identifying a number of HS-PMSM configurations that comply with both design targets and operating constraints. Among these, the most suitable configuration can be selected by means of an appropriate optimization criterion. In particular, the best HS-PMSM configuration has been achieved by minimizing PM thickness. The results achieved by the proposed analytical multi-parameter design procedure have been compared with those achieved by extensive Finite Element Analyses (FEAs) that have regarded both mechanical and electromagnetic aspects. The comparison reveals a very

good agreement between analytical and FEA results, although some minor differences occur, which are related mainly to the assumptions made for achieving a simplified electromagnetic model of the HS-PMSM. However, these differences do not impair the effectiveness of the proposed procedure, which aims to be a supporting tool for a fast but still preliminary HS-PMSM design.

Regarding the HS-PMSM control approach, the three-phase-on control strategy (3PO) already proposed in the literature for Permanent Magnet Brushless DC Machine (PMBDCM) has been considered at first, based on which an improved control strategy has been developed. The improvement consists of injecting an appropriate zero-sequence current component that enables a further reduction of Joule losses compared to those achievable by means of the original 3PO. Furthermore, a suitable Space Vector Control (SVC) has been developed by defining a novel *ft* synchronous reference frame for PMBDCM, similar to the well-known *dq* reference frame employed for Permanent Magnet Brushless AC Machines (PMBACMs). As a result, both field and torque current components can be clearly identified. An appropriate look-up table has been also defined in order to synthetize the *ft* reference current components in accordance with both reference torque and actual speed values, as well as with PMBDCM operating constraints. This has enabled PMBDCM flux weakening operation and, thus, extended constant power operation and high maximum speed. Reference current tracking has been guaranteed by a simple PI-based control system, which has been designed in the novel *ft* synchronous reference frame. The effectiveness of the proposed SVC applied to the designed HS-PMSM in comparison with a conventional Current Commutation Control (CCC) has been verified through numerical simulations, which have been carried out in the Matlab Simulink environment. These reveal very good performances achieved by SVC at any operating condition, but especially in terms of average torque, torque ripple, constant power operation, Joule losses and maximum speed.

V. REFERENCES

[1] T. F. Chan and L. L. Lai, "Permanent-Magnet Machines for Distributed Power Generation: A Review," in *Proc. of IEEE Power Engineering Society General Meeting (2007)*, Tampa (USA), 2007, pp. 1–6.

[2] A. M. El-Refaie, "Motors/generators for traction/propulsion applications: A review," *IEEE Veh. Technol. Mag.*, vol. 8, no. 1, pp. 90–99, Mar. 2013.

[3] S. O. Ani, D. Bang, H. Polinder, J. Y. Lee, S. R. Moon, and D. H. Koo, "Human powered axial flux permanent magnet machines: Review and comparison," in *Proc. of 2nd IEEE Energy Conversion Congress and Exposition (ECCE 2010)*, 2010, pp. 4165–4170.

[4] K. T. Chau, C. C. Chan, and C. Liu, "Overview of Permanent-Magnet Brushless Drives for Electric and Hybrid Electric Vehicles," *IEEE Trans. Ind. Electron.*, vol. 55, no. 6, pp. 2246–2257, Jun. 2008.

[5] R. Krishnan, *Permanent Magnet Synchronous and Brushless DC Motor Drives*. New York: CRC Press, 2010.

[6] M. Cheng, W. Hua, J. Zhang, and W. Zhao, "Overview of Stator-Permanent Magnet Brushless Machines," *IEEE Trans. Ind. Electron.*, vol. 58, no. 11, pp. 5087–5101, Nov. 2011.

[7] A. M. El-Refaie, "Fault-tolerant permanent magnet machines: a review," *IET Electr. Power Appl.*, vol. 5, no. 1, pp. 59–74, Jan. 2011.

[8] K. H. Kim, H. I. Park, S. M. Jang, D. J. You, and J. Y. Choi, "Comparative Study of Electromagnetic Performance of High-Speed Synchronous Motors With Rare-Earth and Ferrite Permanent Magnets," *IEEE Trans. Magn.*, vol. 52, no. 7, pp. 1–4, Jul. 2016.

[9] M. Kimiabeigi *et al.*, "High-Performance Low-Cost Electric Motor for Electric Vehicles Using Ferrite Magnets," *IEEE Trans. Ind. Electron.*, vol. 63, no. 1, pp. 113–122, Jan. 2016.

[10] I. Boldea, L. N. Tutelea, L. Parsa, and D. Dorrell, "Automotive Electric Propulsion Systems With Reduced or No Permanent Magnets: An Overview," *IEEE Trans. Ind. Electron.*, vol. 61, no. 10, pp. 5696–5711, Oct. 2014.

[11] F. Martin, A. Belahcen, and M. E. H. Zaïm, “Effect of magnet materials on optimal design of a high speed PMSM,” in *Proc. of 18th International Conference on Electrical Machines and Systems (ICEMS 2015)*, Pattaya (Thailand), 2015, pp. 661–667.
[12] R. R. Moghaddam, “High speed operation of electrical machines, a review on technology, benefits and challenges,” in *Proc. of IEEE Energy Conversion Congress and Exposition (ECCE 2014)*, Pittsburgh (USA), 2014, pp. 5539–5546.
[13] W. Gengji, Q. Qinglei, W. Ping, and W. Xiaoyuan, “Analysis of the rotor loss in a high speed permanent magnet motor for flywheel energy storage system,” in *Proc. of 18th International Conference on Electrical Machines and Systems (ICEMS 2015)*, Pattaya (Thailand), 2015, pp. 2040–2044.
[14] Z. Kolondzovski, A. Arkkio, J. Larjola, and P. Sallinen, “Power Limits of High-Speed Permanent-Magnet Electrical Machines for Compressor Applications,” *IEEE Trans. Energy Convers.*, vol. 26, no. 1, pp. 73–82, Mar. 2011.
[15] A. Tenconi, S. Vaschetto, and A. Vigliani, “Electrical Machines for High-Speed Applications: Design Considerations and Tradeoffs,” *IEEE Trans. Ind. Electron.*, vol. 61, no. 6, pp. 3022–3029, Jun. 2014.
[16] A. Rezzoug and M. E.-H. Zaim, Eds., *Non-conventional Electrical Machines*, 1 edition. Wiley-ISTE, 2013.
[17] D. Gerada, A. Mebarki, N. L. Brown, C. Gerada, A. Cavagnino, and A. Boglietti, “High-Speed Electrical Machines: Technologies, Trends, and Developments,” *IEEE Trans. Ind. Electron.*, vol. 61, no. 6, pp. 2946–2959, Jun. 2014.
[18] D. Fodorean, “State of the Art of Magnetic Gears, their Design, and Characteristics with Respect to EV Application,” in *Modeling and Simulation for Electric Vehicle Applications*, InTech, 2016, pp. 73–95.
[19] M. Miyamasu and K. Akatsu, “Efficiency comparison between Brushless dc motor and Brushless AC motor considering driving method and machine design,” in *IECON 2011 - 37th Annual Conference on IEEE Industrial Electronics Society*, 2011, pp. 1830–1835.
[20] Y. F. Shi, Z. Q. Zhu, and D. Howe, “Torque-Speed Characteristics of Interior-Magnet Machines in Brushless AC and DC Modes, with Particular Reference to Their Flux-Weakening Performance,” in *Power Electronics and Motion Control Conference, 2006. IPEMC 2006. CES/IEEE 5th International*, 2006, vol. 3, pp. 1–5.
[21] Z. Q. Zhu, J. X. Shen, and D. Howe, “Flux-Weakening Characteristics of Trapezoidal Back-EMF Machines in Brushless DC and AC Modes,” in *Power Electronics and Motion Control Conference, 2006. IPEMC 2006. CES/IEEE 5th International*, 2006, vol. 2, pp. 1–5.
[22] Y. Liu, Z. Q. Zhu, and D. Howe, “Commutation-Torque-Ripple Minimization in Direct-Torque-Controlled PM Brushless DC Drives,” *IEEE Trans. Ind. Appl.*, vol. 43, no. 4, pp. 1012–1021, Jul. 2007.
[23] T. Shi, Y. Guo, P. Song, and C. Xia, “A New Approach of Minimizing Commutation Torque Ripple for Brushless DC Motor Based on DC-DC Converter,” *IEEE Trans. Ind. Electron.*, vol. 57, no. 10, pp. 3483–3490, Oct. 2010.
[24] J. Shi and T. C. Li, “New Method to Eliminate Commutation Torque Ripple of Brushless DC Motor With Minimum Commutation Time,” *IEEE Trans. Ind. Electron.*, vol. 60, no. 6, pp. 2139–2146, Jun. 2013.
[25] C. Xia, Y. Xiao, W. Chen, and T. Shi, “Torque Ripple Reduction in Brushless DC Drives Based on Reference Current Optimization Using Integral Variable Structure Control,” *IEEE Trans. Ind. Electron.*, vol. 61, no. 2, pp. 738–752, Feb. 2014.
[26] T. Kim, H.-W. Lee, L. Parsa, and M. Ehsani, “Optimal Power and Torque Control of a Brushless DC (BLDC) Motor/Generator Drive in Electric and Hybrid Electric Vehicles,” in *Conference Record of the 2006 IEEE Industry Applications Conference, 2006. 41st IAS Annual Meeting*, 2006, vol. 3, pp. 1276–1281.
[27] G. Gatto, I. Marongiu, A. Perfetto, and A. Serpi, “Three-Phase Operation of Brushless DC Motor Drive Controlled by a Predictive Algorithm,” in *Proc. of 32nd Annual Conference on IEEE Industrial Electronics (IECON 2006)*, 2006, pp. 1166–1170.

[28] A. Damiano *et al.*, “Performance comparison between two-phase-on and three-phase-on operation of Brushless DC drives,” in *Proc. of 21st International Symposium on Power Electronics, Electrical Drives, Automation and Motion (SPEEDAM 2014)*, Ischia (Italy), 2014, pp. 489–494.
[29] G. Gatto, I. Marongiu, A. Perfetto, and A. Serpi, “Sensorless brushless DC drive controlled by predictive algorithm,” in *Proc. of 35th Annual Conference of IEEE Industrial Electronics (IECON 2009)*, Porto (Portugal), 2009, pp. 1270–1275.
[30] G. Brando, A. D. Pizzo, G. Gatto, I. Marongiu, and A. Serpi, “Permanent magnet brushless drives controlled by sensorless predictive algorithm,” in *2010 XIX International Conference on Electrical Machines (ICEM)*, 2010, pp. 1–6.
[31] A. Binder, T. Schneider, and M. Klohr, “Fixation of buried and surface-mounted magnets in high-speed permanent-magnet synchronous machines,” *IEEE Trans. Ind. Appl.*, vol. 42, no. 4, pp. 1031–1037, Jul. 2006.
[32] F. Zhang, G. Du, T. Wang, G. Liu, and W. Cao, “Rotor Retaining Sleeve Design for a 1.12-MW High-Speed PM Machine,” *IEEE Trans. Ind. Appl.*, vol. 51, no. 5, pp. 3675–3685, Sep. 2015.
[33] Z. Kolondzovski, A. Belahcen, and A. Arkkio, “Comparative thermal analysis of different rotor types for a high-speed permanent-magnet electrical machine,” *IET Electr. Power Appl.*, vol. 3, no. 4, pp. 279–288, Jul. 2009.
[34] R. C. Juvinall and K. M. Marshek, *Fundamentals of Machine Component Design*, 5 Har/Psc edizione. Hoboken, NJ: John Wiley & Sons Inc, 2011.
[35] “Car Configurator Volkswagen: per configurare come vuoi la tua prossima auto!” [Online]. Available: https://www.volkswagen.it/content/vw_pkw/importers/it/it/configurator.html. [Accessed: 17-Jan-2018].
[36] A. Serpi, “A flux-weakening predictive control algorithm for extended constant-power operation of surface-mounted PM machines,” in *Proc. of 20th International Conference on Electrical Machines (ICEM 2014)*, Berlin (Germany), 2014, pp. 658–664.
[37] Z. Huang and J. Fang, “Multi-Physics Design and Optimization of High Speed Permanent Magnet Electrical Machines for Air Blower Applications,” *IEEE Trans. Ind. Electron.*, vol. PP, no. 99, pp. 1–1, 2016.
[38] M. Mirzaei and A. Binder, “Permanent magnet savings in high speed electrical motors,” in *International Symposium on Power Electronics, Electrical Drives, Automation and Motion, 2008. SPEEDAM 2008*, 2008, pp. 1276–1281.
[39] Vacuumschmelze Gmbh & Co., “VACOFLUX Magnetic Properties.” [Online]. Available: http://www.vacuumschmelze.com/en/products/materials-parts/soft-magnetic/cobalt-iron/vacoflux/vacoflux-magnetic-properties.html. [Accessed: 21-Oct-2016].
[40] M. van der Geest, H. Polinder, J. A. Ferreira, and D. Zeilstra, “Stator winding proximity loss reduction techniques in high speed electrical machines,” in *Electric Machines Drives Conference (IEMDC), 2013 IEEE International*, 2013, pp. 340–346.
[41] J. F. Gieras, “Design of permanent magnet brushless motors for high speed applications,” in *Proc. of 17th International Conference on Electrical Machines and Systems (ICEMS 2014)*, Hangzhou (China), 2014, pp. 1–16.
[42] H. Katagiri *et al.*, “Fast calculation method of AC copper loss for high speed machines,” in *2016 19th International Conference on Electrical Machines and Systems (ICEMS)*, 2016, pp. 1–6.
[43] U.S. Department of Energy (DOE), “Vehicle Technologies Office: 2015 Electric Drive Technologies Annual R&D Progress Report | Department of Energy,” 2015.
[44] P. Moreno-Torres, M. Lafoz, M. Blanco, and J. R.Arribas, “Passenger Exposure to Magnetic Fields in Electric Vehicles,” in *Modeling and Simulation for Electric Vehicle Applications*, InTech, 2016, pp. 47–71.
[45] H. W. Jun, J. Lee, H. W. Lee, and W. H. Kim, “Study on the Optimal Rotor Retaining Sleeve Structure for the Reduction of Eddy-Current Loss in High-Speed SPMSM,” *IEEE Trans. Magn.*, vol. 51, no. 3, pp. 1–4, Mar. 2015.

[46] Y. Xia, J. Li, R. Qu, and H. Fang, “Comparison of two rotor topologies for high-speed permanent magnet synchronous machines,” in *2016 XXII International Conference on Electrical Machines (ICEM)*, 2016, pp. 1419–1425.
[47] A. Serpi, G. Fois, F. Deiana, G. Gatto, and I. Marongiu, “Performance improvement of brushless DC machine by zero-sequence current injection,” in *Proc. of 41st Annual Conference of the IEEE Industrial Electronics Society (IECON 2015)*, 2015, pp. 003804–003809.
[48] G. Gatto, I. Marongiu, A. Perfetto, and A. Serpi, “Brushless DC generator controlled by constrained predictive algorithm,” in *Proc. of 19th IEEE International Symposium on Industrial Electronics (ISIE 2010)*, Bari (Italy), 2010, pp. 1224–1229.
[49] A. Serpi, “Predictive control of electrical drives,” Tesi di dottorato, Universita’ degli Studi di Cagliari, 2009.

VI. PUBLICATIONS

- A. Serpi, G. Fois, F. Deiana, G. Gatto, I. Marongiu, "Performance Improvement of Brushless DC Machine by Zero-Sequence Current Injection", in Proc. *41st Annual Conference of IEEE Industrial Electronics*, Nov. 9-12, 2015.
- A. Damiano, A. Floris, G. Fois, I. Marongiu, M. Porru, A. Serpi, "Design of a High-Speed Ferrite-based Brushless DC Machine for Electric Vehicles", in Proc. *XXII International Conference on Electrical Machines ICEM2016*, Lausanne (Switzerland), Sept. 4-7, 2016.
- A. Damiano, G. Fois, I. Marongiu, M. Porru, A. Serpi, "Space Vector Control of Permanent Magnet Brushless DC Machines", in Proc. *XXII International Conference on Electrical Machines ICEM2016*, Lausanne (Switzerland), September 4th-7th, 2016
- A. Damiano, A. Floris, G. Fois, M. Porru, A. Serpi, "Modeling and Design of PM Retention Sleeves for High-Speed PM Synchronous Machines", in Proc. *6th International Electric Drives Prodution Conference and Exhibition 2016*, Numberg (Germany), Nov. 30th – Dec. 1st, 2016.
- A. Damiano, A. Floris, G. Fois, I. Marongiu, M. Porru, A. Serpi, "Design of a High-Speed Ferrite-based Brushless DC Machine for Electric Vehicles", in *IEEE Transaction on Industry Applications*, volume 53 pp.4279-4287, Sept.-Oct 2017
- G. Fois, A. Floris, A. Serpi, M. Porru, A. Damiano, "Design Criteria for High-Speed Ferrite-Based Permanent Magnet Synchronous Machines", in Proc. *7th International Electric Drives Production Conference and Exhibition 2017*, Würzburg (Germany), Dec. 5-6, 2017.